A THREE DIMENSIONAL MODEL OF ATMOSPHERIC CO_2 TRANSPORT BASED ON OBSERVED WINDS:
3. SEASONAL CYCLE AND SYNOPTIC TIME SCALE VARIATIONS

Martin Heimann,[1] Charles D. Keeling,[2] and Compton J. Tucker[3]

Abstract. The spatial and temporal distribution of atmospheric CO_2 and of its $^{13}C/^{12}C$ ratio have been simulated with a three-dimensional atmospheric transport model based on the observed wind fields of the Global Weather Experiment in 1978/1979. Modeled sources and sinks of carbon at the surface of the Earth include: (1) CO_2 released from fossil fuel combustion, (2) exchange of CO_2 with the terrestrial biosphere by specification of net primary productivity from satellite data and heterotrophic respiration from surface temperature, (3) air-sea exchange of CO_2 driven by prescribed temporal and spatial variations of CO_2 in the surface waters. The relative contributions of individual source components are calculated by running the model with each component separately. This paper describes the results of the model simulations in terms of the seasonal cycle and synoptic time scale variations. Acceptable agreement with observations is achieved for northern hemisphere and tropical stations. In the southern hemisphere the model overestimates the observed seasonal cycle. The relationship between the $^{13}C/^{12}C$ isotopic ratio and CO_2 concentration is discussed as a potential means to distinguish biological and oceanic contributions to the seasonal cycle.

1. Introduction

Atmospheric CO_2 concentrations vary systematically with season as a result of the direct removal of CO_2 from the air during photosynthesis of land plants and the emission of CO_2 to the air by the respiration of land plants and their detritus including soils. Wherever the growing season is reduced or interrupted in winter, the uptake of CO_2 is more strongly seasonal than respiration so that a net drawdown of atmospheric CO_2 occurs during the main growing season in summer, and a net release during the rest of the year. The difference between the fluxes arising from photosynthesis and respiration is reflected in an annual oscillation in atmospheric CO_2. This seasonal oscillation is observable almost everywhere in the lower atmosphere because the vigorous circulation of the atmosphere propagates the seasonal cycle even to regions remote from direct seasonal plant activity, for example, to the air above the oceans and to the geographic poles.

The oceanic carbon cycle also contributes to the seasonality of atmospheric CO_2 owing to temperature variations that affect the partial pressure exerted by CO_2 gas dissolved in surface waters, upwelling and downwelling of waters with different carbon contents which cause variable exchange of carbon-bearing compounds between surface and subsurface water, the metabolic activity of marine organisms, and the oxidation of organic remains which withdraw and release CO_2 in the near surface water. The seasonally varying biological cycle in the oceans is of comparable magnitude to that on land, but the influence of this cycle on atmospheric CO_2 is greatly attenuated because of the relatively slow exchange of CO_2 occurring at the air-sea boundary. In the southern hemisphere the seasonal CO_2 signal from land plants is much smaller than in the northern hemisphere as a result of the smaller land area exhibiting seasonal growing seasons. Here the oceanic contribution to atmospheric CO_2 approaches the magnitude of the terrestrial biospheric contribution.

To some extent stationary sources and sinks also contribute to the seasonality of atmospheric CO_2, especially where atmospheric transport is strongly seasonal, for example in the tropics. Finally, man-induced CO_2 fluxes, especially the combustion of fossil fuels, exhibit some seasonality, and even their steady component produces a non-negligible seasonal atmospheric CO_2 signal owing to seasonal atmospheric transport.

Isotopic measurements provide a means to distinguish oceanic and terrestrial biospheric contributions to the seasonal cycle of atmospheric CO_2, as noted by Keeling et al. [this volume, a]. The terrestrial biospheric seasonal signal is accompanied by fractionation of the rare isotope, ^{13}C, relative to the abundant isotope, ^{12}C. This fractionation produces a shift in the $^{13}C/^{12}C$ ratio of atmospheric CO_2 which closely correlates with concentration variations. The isotopic seasonal signal from the oceans, on the other hand, is almost negligible [Siegenthaler and Münnich, 1981]. Since fossil fuel contains carbon principally of plant origin, its isotopic composition is nearly the same as carbon from present day land plants. As a consequence the observed isotopic seasonal signal of atmospheric CO_2, although mainly owing to the activity of land plants, contains a non-negligible contribution from the seasonal signal produced by the combustion of fossil fuels.

The atmospheric CO_2 concentration and isotopic data provide, by themselves, some quantitative information on the seasonal carbon cycle. For example, owing to the predominance of seasonality

[1]Max-Planck-Institut für Meteorologie, Bundesstrasse 55 D-2000 Hamburg 13, FRG
[2]Scripps Institution of Oceanography, La Jolla, CA, 92093, U.S.A.
[3]NASA/GSFC, Greenbelt, MD, 20771, U.S.A.

in the northern hemisphere and the weak exchange of signals across the equator, it is possible to estimate roughly the overall seasonal drawdown of CO$_2$ in each hemisphere by direct integration of atmospheric CO$_2$ records. A far more satisfactory accounting of the sources and sinks of atmospheric CO$_2$ can be accomplished, however, by employing a realistic representation of the three-dimensional circulation of the atmosphere.

In this and in the accompanying article [Keeling et al., this volume, b] we describe the results of a tracer modeling study aimed at reproducing the spatial and temporal features of the atmospheric cycle of CO$_2$ and its ^{13}C/^{12}C stable isotope ratio, both features averaged over one or more years. We employed a three-dimensional transport model of the global troposphere based on the observed wind fields approximately of the year 1979, coupled to a two-dimensional, time-dependent prescription of the atmospheric CO$_2$ sources and sinks at the surface of the Earth.

In particular our two articles jointly address the following four questions:

(1) Is the observed spatial and temporal distribution of atmospheric CO$_2$ and its ^{13}C/^{12}C ratio consistent with current knowledge about sources and sinks?

(2) What are the concentration patterns generated by individual parts of the carbon cycle such as the terrestrial biosphere and the surface layer of the ocean?

(3) How do individual CO$_2$ sources and sinks affect observed concentrations at the major observing locations?

(4) Which part of the observed temporal and spatial variability of the CO$_2$ concentration is produced by the atmospheric circulation alone?

These questions have been addressed before in several modeling studies by means of multidimensional models of the atmosphere. Most notably, Fung et al. [1983, 1987] investigated the three-dimensional structure of the seasonal signal generated by the terrestrial biosphere alone. Their study was extended by inclusion of seasonal exchanges of CO$_2$ with the upper ocean by Fung [1986]. Using two-dimensional models of the atmosphere (with latitudinal and vertical resolution), Pearman and Hyson [1980], Pearman et al. [1983], Pearman and Hyson [1986], Enting and Mansbridge [1989], and Tans et al. [1989] assessed the contributions of all identified components affecting the atmospheric concentration of CO$_2$ and its stable isotopic ratio. The present study represents an extension of a three-dimensional study by Heimann et al. [1986].

The present article contains the analysis of the simulation results on time scales up to 1 year, including the seasonal cycle and synoptic scale short-term variations. The discussion of the mean annual concentration fields is deferred to the succeeding article by Keeling et al. [this volume, b]. In the next section we present a brief description of the transport model; section 3 summarizes the simulated sources of CO$_2$ used in the model runs, and section 4 describes the CO$_2$ data to which the model results are compared in section 5.

2.   The Transport Model

The three-dimensional atmospheric tracer model used in the present study is described in detail by Heimann and Keeling [this volume]. It has a horizontal resolution of approximately 8° latitude by 10° longitude, 9 layers in the vertical dimension, and a numerical time step of 4 hours. The tracer is advected by three-dimensional, time-dependent wind fields and is mixed vertically by convection. The model uses no explicit horizontal diffusion. The wind fields were derived from the meteorological fields obtained during the GWE (Global Weather Experiment) from December 1978 through November 1979.

The parameterization of vertical convection (including all scales of motion which are not resolved in the wind fields on the model grid) is described by a set of monthly transition matrices. They were retained from a previous version of the tracer model, which used wind fields generated from a three-dimensional general circulation model (GCM) of the atmosphere developed for climate studies by Hansen et al. [1983]. Based on a preliminary investigation of the attenuation of the seasonal cycles of CO$_2$ with height, we reduced the convective matrices globally to 0.50 of their original values. As a sensitivity case we repeated each simulation with the matrices set globally to 0.25 of their original values. Unless noted otherwise, however, all results shown refer to the standard case of 0.50 reduction.

For the simulation of the concentration distribution of tracers the model is repeatedly cycled through the wind fields of the GWE year. Simulations of the chemically inert radioactive trace gases ^{85}Kr and ^{222}Rn, as described by Heimann and Keeling [this volume], show that the model quite closely reproduces the distribution of gaseous tracers with life-times greater than a few days.

3.   Simulated Sources and Sinks

3.1   Modeling Strategy

The aim of this seasonal tracer modeling study is to simulate the atmospheric carbon cycle as it existed during the 2-year time period, 1979–1980, for which Keeling et al. [this volume, a] have assembled a set of atmospheric CO$_2$ data specifically for use in this study. To this end we adopted the following strategy.

Firstly, we assume that the natural carbon cycle during this period was, on annual average, at a steady state. Hence we assume that all natural atmospheric carbon source/sink terms were then either locally or globally balanced over the course of 1 year.

Superimposed on this assumed steady state are perturbation fluxes of carbon which have been induced by human activities, most notably by the release of CO$_2$ from fossil fuel combustion. To assess the magnitudes of these perturbation fluxes we resort to a global carbon cycle compartment model, which was run over the whole industrial era [Keeling et al., this volume, a]. The perturbation fluxes predicted by this model for the time period of 1979–1980 are then introduced as time invariant sources and sinks into the three-dimensional tracer model, except that in the case of industrial CO$_2$ emissions a small seasonal variation is also included in the specification of the source. Hence the simulated annually averaged increase of the atmospheric CO$_2$ concentration is specified a priori from the assumed strength of the perturbation sources and sinks. The distribution of CO$_2$ in the atmosphere is therefore assumed to prevail at a quasi-stationary state.

The total carbon source/sinks at the earth's surface were divided into nine source components, and the transport model was run with each of the components separately. The different components are listed with their main characteristics in Table 1, copied from Table 4 of Heimann and Keeling [this volume]. Details of the procedures used to construct these source/sink functions are described in Heimann and Keeling [this volume].

TABLE 1. CO_2 Source Components Used in the Three Dimensional Atmospheric CO_2 Transport Model

1. Seasonal -- locally balanced

   1.   Net primary productivity of the terrestrial biosphere

   2.   Heterotrophic respiration of the terrestrial biosphere

   3.   Air-sea exchange driven by seasonally varying oceanic pCO_2

   4.*   Temperature dependent isotopic fractionation associated with CO_2 exchange at the ocean surface

2. Time independent -- globally balanced

   5.   Equatorial oceanic pCO_2 source balanced by equal and uniform oceanic sinks poleward of approximately $16°$ in each hemisphere

   6.   An oceanic source south of approximately $39°S.$, balanced by a sink in the Atlantic Ocean north of approximately $23°N.$

3. Seasonally ranging or time independent -- net releases or uptakes

   7.   Industrial CO_2 from fossil fuel combustion and cement production

   8.   Release of CO_2 by changes in land use and by deforestation

   9.   Uptake of CO_2 by the terrestrial biosphere in proportion to annual net primary productivity

   10.   Uptake of CO_2 by the oceans at a uniform rate per unit area of ice-free ocean surface

   11.* Isotopic exchange between the atmosphere and oceans associated with industrial CO_2 release and the unbalanced terrestrial biosphere (Carbon-13 Suess effect)

*Component has no concentration dependency.

Here, we review briefly these source components, with emphasis on those that vary in time during the course of the year. These are the exchange fluxes of net primary productivity and of heterotrophic respiration due to the terrestrial biosphere, the seasonal exchanges of CO_2 between the atmosphere and the surface ocean waters, and the release of industrial CO_2 from fossil fuel combustion and cement production. All other source components are assumed to be steady in time, hence their contributions to the combined seasonal model signal are small at most places, as they result primarily from seasonally changing features of the atmospheric circulation.

In order to compare the overall strength of seasonal sources, we define the seasonal net carbon transfer (SNCT) produced by a source flux $F(\mathbf{x},t)$ (expressed in kgC m^{-2} yr^{-1}) as a function of time, t, in an area A as follows

$$SNCT(A) = 0.5 \int_{\Delta t} \left| \int_A (F(\mathbf{x},t) - \overline{F}(\mathbf{x})) dA \right| dt \qquad (3.1)$$

where $\overline{F}(\mathbf{x})$ denotes the flux averaged over the base interval $\Delta t = 1$ yr at location $\mathbf{x}$ ($\equiv x,y,z$, the three Cartesian space coordinates).

The SNCT is not additive, i.e., in general

$$SNCT(A \cup B) \le SNCT(A) + SNCT(B) \qquad (3.2)$$

the equality being true only if the source flux $F(\mathbf{x},t)$ exhibits the same time dependence in region B as in region A. Since the carbon exchange fluxes in our model display opposite phases in the two hemispheres, we quote values of the SNCT for each hemisphere, and also for the tropical and temperate latitudes, separated at approximately $23°N.$ and $23°S.$, respectively.

For the terrestrial biosphere, in the case of a unimodal time variation of the flux $F(\mathbf{x},t)$, the SNCT is equivalent to the "growing season net flux" (GSNF) defined by Fung et al. [1983] or to the "net ecosystem production per growing season" of Pearman and Hyson [1983], representing the net amount of carbon transferred to the terrestrial biosphere during the growing season.

Our proposed definition of the SNCT extends, however, to other time dependent source fluxes as well. In view of inequality (3.2) care must be exercised in comparing our estimates of SNCT with other estimates.

3.2 Exchanges of CO_2 with the Terrestrial Biosphere

As described in detail by Heimann and Keeling [this volume], the seasonal exchange flux of CO_2 between the atmosphere and the terrestrial biosphere is modeled as the sum of two components. One of these represents net primary productivity due to photosynthesis; the other represents the flux of CO_2 resulting from decomposition of organic material, mainly by heterotrophic respiration.

Net primary productivity (NPP) is estimated by means of a model for remote sensing of plant growth by Kumar and Monteith [1981]. This model allows the calculation of CO_2 uptake by a plant canopy from remotely sensed data of the reflectivity of the canopy-soil system in two spectral windows, and from the photosynthetically active solar radiation (direct and diffuse) impinging on the canopy.

Data of two channels of the Advanced Very High Resolution Radiometer (AVHRR) from the time period of November 1983 through October 1984 were used to derive monthly averaged reflectivities of the soil-canopy system. Insolation was calculated from astronomical formulas in conjunction with an empirical relationship describing the attenuation of solar radiation by cloud cover.

Heterotrophic respiration is represented in the model by two parts, one assumed to be constant in time, the other assumed to be controlled by ground temperature. For the latter we assumed an exponential relationship with an increase in the flux of 50 percent for a surface air temperature increase of $10°C$. The temperature data, derived from the Global Weather Experiment, were for the period November 1978 through October 1979. The sum of the two parts of the respiration function, integrated over 1 year, was set to be equal in magnitude to the annual NPP at each location; hence we assumed the biosphere to be locally balanced over each annual cycle.

The magnitude of the temperature-dependent part of the respiratory flux relative to the constant part was left as an adjustable global parameter that was determined by a weighted fit of the results of the model simulated CO_2 concentrations to the observed seasonal variation in concentration at four northern hemisphere stations: Point Barrow, Alaska, (PTB) at $71°N.$, $157°W.$; Ocean Sta-

TABLE 2. Harmonic Coefficients of the Observed Seasonal Variation (in ppm)
at the Four Calibrating Stations in the Northern Hemisphere for 1980

Harmonic	Point Barrow(PTB) (71°N.,157°W.)		Ocean Station P (STP) (50°N.,144°W.)		La Jolla(LJO) (33°N.,117°W.)		Cape Kumukahi(KUM) (20°N.,155°W.)	
1	2.44207	6.16903	1.14166	4.86968	0.89265	3.90509	−0.26411	3.50410
	0.11322	0.20942	0.07603	0.16936	0.08146	0.16957	0.06908	0.06600
2	1.19095	−2.68750	0.52065	−2.54184	0.47178	−1.61584	0.66978	−1.11080
	0.09051	0.12239	0.06736	0.10494	0.07436	0.09962	0.06622	0.06909
3	−0.76321	0.74696	−0.57754	0.33618	−0.19089	0.43714	−0.16672	0.17411
	0.08604	0.08900	0.06954	0.06689	0.07034	0.07221	0.06753	0.06785
4	0.25300	−0.26476	0.05275	0.13811	−0.02961	0.20866	−0.07504	−0.01989
	0.08354	0.08476	0.06672	0.06636	0.06815	0.07035	0.06729	0.06747

Note

Numbers in the first row of each harmonic denote coefficients of cosine and sine term, respectively; numbers in the second row denote estimate of the standard deviation of coefficient above, also expressed in ppm.

tion P, (STP) at 50°N., 144°W.; La Jolla, California, (LJO) at 33°N., 117°W.; and Cape Kumukahi, Hawaii, (KUM) at 20°N., 155°W. These observational data are listed in Table 2 in ppm (parts per million of dry air by volume). As a result we obtained a relative magnitude 0.69, with a standard error of 0.07, for the temperature dependent part of the respiratory flux. This result depends on the assumed strength of the subgridscale vertical convective parameterization, which for the standard case was set to 0.50 of the original values [Heimann and Keeling, this volume]. As a sensitivity case we also ran the model where we set the convective parameterization to 0.25 of its original values. In this case a relative magnitude of 0.77, with a standard error of 0.07, for the temperature-dependent part of the respiratory flux yields an optimal fit to the observations at the four northern hemisphere stations. Details of the fitting procedure are presented in Appendix D of Heimann and Keeling [this volume]. The fitting factors were rounded to exactly 0.69 and 0.77 to produce the composite CO_2 fields used in our subsequent analysis.

Since the temperature data used to establish the temperature dependent part of the respiratory flux are approximately for the calendar year 1979, and the atmospheric CO_2 data used in the fitting procedure are for the average of 1979 and 1980, the estimation of respiration would properly apply to an annual period near January 1, 1980, were it not that the annual integral of respiration for each location is determined from NPP, derived from remote-sensing data for approximately the year 1984. Thus our representation of respiration does not represent either the actual conditions for a single year or the average over several years. Because the seasonal cycle of atmospheric CO_2, apart from changes in peak-to-peak amplitude, varies only slightly from year to year, this use of data for different recent time periods probably does not introduce serious errors into our analysis. It is, however, a future goal to obtain contemporary data for all parameters.

In addition to the seasonally balanced fluxes of NPP and respiration, two additional fluxes to and from the terrestrial biosphere have been simulated in the model: a global net input flux of 1.7910×10^{12} kgC yr^{-1}, which we call "biospheric destruction," resulting from anthropogenic changes in land use and deforestation, and a net uptake flux of 2.1037×10^{12} kgC yr^{-1}, which we call "biospheric fertilization," owing to CO_2 stimulated growth of the biosphere. Biospheric destruction was estimated in magnitude

and regional distribution by Houghton et al. [1987] for the year 1980, while biospheric fertilization was estimated from the global carbon cycle model, also for 1980 [Keeling et al., this volume, a]. Both fluxes are assumed to be constant in time in the simulations. Because of their small magnitude compared to the seasonal biospheric fluxes, they do not induce any significant seasonal CO_2 concentration patterns.

As an example of the seasonal cycle of NPP as derived by our modeling procedures we compare in Figure 1 the inferred seasonal NPP over the British Isles and Europe at 50°N., near 0°E. (England) and 20°E. (Poland). (All fluxes here and in the next several figures are expressed in gC month^{-1} m^{-2} of land area). There is a clear difference between the two sites, the latter having a more continental character as displayed by a shorter vegetation period which is delayed by almost a whole month with respect to the former.

As a further illustration we display in Figure 2 the resulting monthly biospheric fluxes along a north-south section at 30°E. over eastern Europe and Africa. Each of the panels shows fluxes
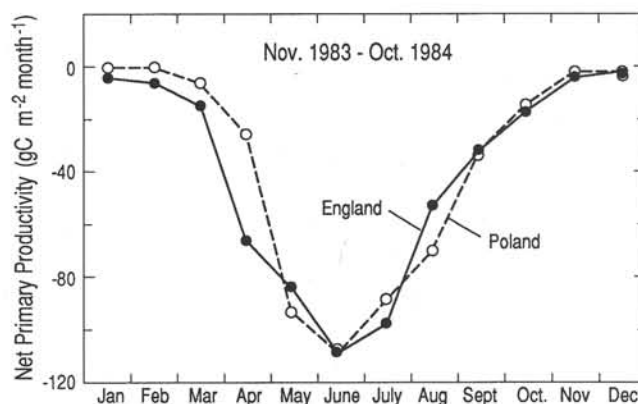

Fig. 1. Monthly averaged net primary productivity approximately over England (model grid box centered at 50°N., 0°E.) and Poland (box centered at 50°N., 20°E.) in gC month^{-1} m^{-2} of land area, based on remote sensing data from November 1983 through October 1984.
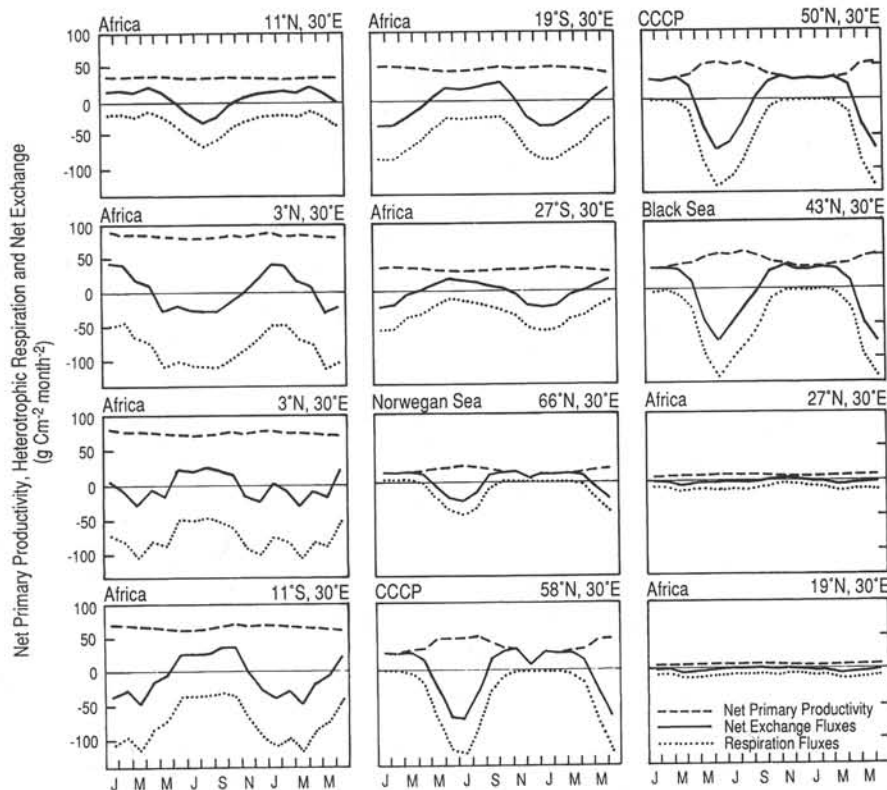
Fig. 2. Net primary productivity, heterotrophic respiration, and net biospheric exchange flux along a north-south section at 30°E. in the same units, and for the same time period, as Figure 1. Each curve represents the flux over land for a grid square of 10° longitude and 7.83° latitude. The first 6 months of each cycle are displayed twice to reveal its annual variation more clearly.

representative of a model grid square of 10.00° longitude and 7.83° latitude. It is seen that substantial seasonal variations exist in the photosynthetic fluxes of the tropical regions of Africa. There is a marked phase change in crossing the equator, as expected from the annual cycle of insolation, rainy season and its associated vegetation period [Tucker et al., 1985]. Near the equator the nearly constant temperatures throughout the year induce no substantial variations into the annual cycle of respiration. North of the desert belt the seasonality of NPP becomes more pronounced. Plant productivity ceasing entirely in the winter months. The respiratory fluxes show distinct seasonal variations, which, however, are smaller than the photosynthetic variations.

Figure 3 summarizes the zonally averaged fluxes of NPP, of respiration, and of the net biospheric exchange as a function of latitude and time of the year as predicted by the model. NPP (see Panel (a)) exhibits a marked seasonal signal in the high latitudes of the northern hemisphere, peaking at around 50°N. early in July. Further to the south the growing season becomes longer in duration, albeit smaller in intensity on zonal average. In the tropical belt maximum NPP follows the annual march of the sun, shown by a solid line, with a delay of 1 to 2 months. This induces substantial seasonal variations in NPP around 10°N. and 10°S., respectively. In the southern hemisphere NPP contrasts quite remarkably with the northern hemisphere. In the zonal average the subtropical

desert belt does not show up, and there is no intensity maximum in the mid-latitudes.

Heterotrophic respiration (see Panel (b)) displays a much weaker seasonality than NPP in the zonal average. The flux in the tropical regions remains almost constant throughout the year.

The zonally averaged net flux of CO_2 (see Panel (c)), defined as positive from the terrestrial biosphere to the atmosphere, exhibits a strong seasonality in the northern hemisphere temperate latitudes, with a marked contrast between the short and intense uptake season and the rest of the year, when the respiratory flux dominates.

This net flux includes contributions from biospheric destruction and fertilization, but they are too small to be readily discernible. Around 50°N. the flux exhibits two local maxima, one in October and one in March, reflecting the influence of temperature on respiration. Substantial seasonal variations occur also in the tropical region, with maximum flux at around 10°N. and 15°S. The net flux south of the equator displays an opposite phase and a quite different time variation compared to the northern hemisphere.

The seasonal net carbon transfer (SNCT) of the terrestrial biosphere source function, according to the model, is 7.14×10^{12} kgC in the northern hemisphere and 1.95×10^{12} kgC in the southern hemisphere (see Table 3). If there were no air mass exchange across the equator, these seasonal biospheric fluxes would result in a hemispherically averaged peak-to-peak concentration variation of
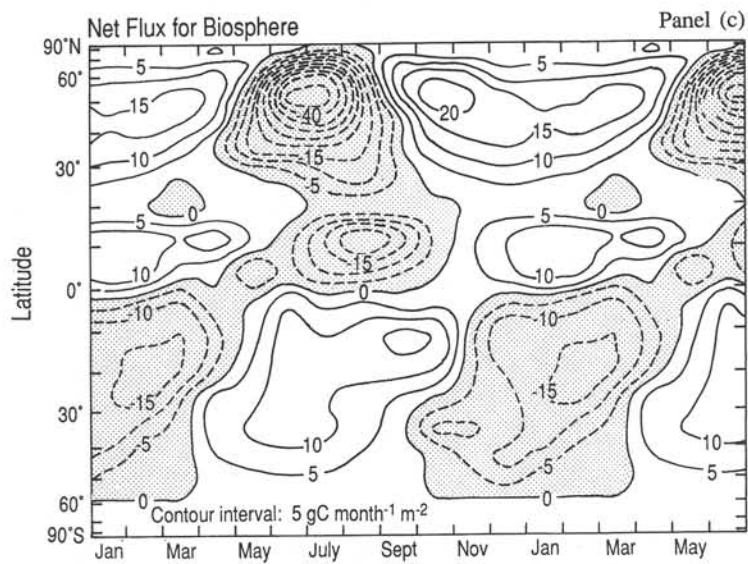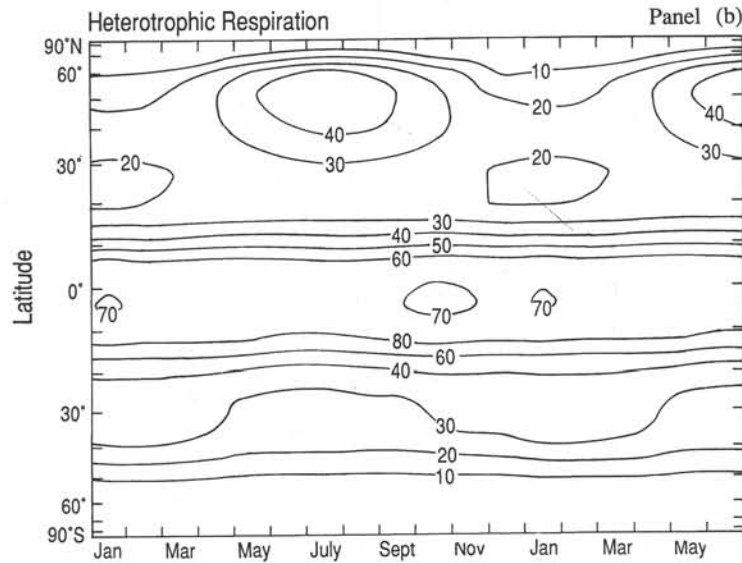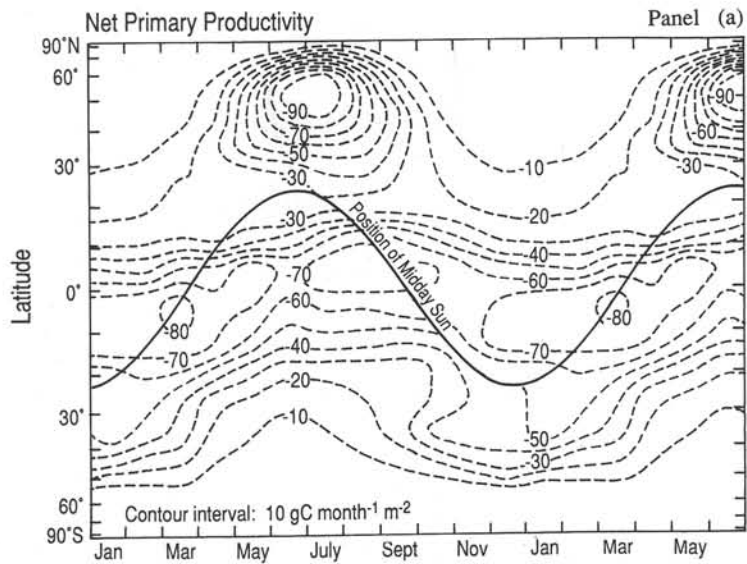
Net Primary Productivity Panel (a)

Contour interval: 10 gC month⁻¹ m⁻²

Heterotrophic Respiration Panel (b)

Net Flux for Biosphere Panel (c)

Contour interval: 5 gC month⁻¹ m⁻²

TABLE 3. Seasonal Net Carbon Transfer (SNCT)
(in 10^{12} kgC)

Zone	Terrestrial Biosphere	Ocean	Industrial CO_2	Total
23°N.-90°N.	6.46	0.47	0.18	7.11
0°-23°N.	0.98	0.18	0.00	1.16
23°S.-0°	1.37	0.32	0.00	1.69
90°S.-23°S.	0.74	0.51	0.06	1.31
Northern hemisphere	7.14	0.64	0.18	7.96
Southern hemisphere	1.95	0.83	0.06	2.84

6.80 parts per million by volume of dry air (ppm) in the northern and 1.86 ppm in the southern hemisphere, respectively.

The magnitude of the SNCT due to the terrestrial biosphere computed here is, of course, directly related to the chosen relative magnitude of the temperature dependent fraction of the respiratory flux. The change is, however, small: if we replaced the value of 0.69, corresponding to the convective parameterization of 50 percent with a value of 0.77, corresponding to a reduction in convective parameterization to 25 percent, we obtain for the SNCT 6.84×10^{12} kgC in the northern and 1.92×10^{12} kgC in the southern hemisphere. Since we prescribe biospheric destruction and fertilization as nonseasonal, these two sources do not contribute to the computations of the biospheric SNCT.

The present approach in establishing the seasonal exchange fluxes of CO_2 between the atmosphere and the terrestrial biosphere in many ways is similar to the one adopted by Fung et al. [1987]. These authors employed a more refined prescription of heterotrophic respiration as a function of surface air temperature for each of four classes of biomes, based on an extensive survey of field studies. Furthermore, they computed the time variation of NPP from essentially the same primary satellite data as used in the present study. The annual integral of NPP, however, was scaled at every grid location to match a global distribution derived from the global vegetation map of Matthews [1983], supplemented by biome specific NPP values. Also, any explicit influence of solar radiation on NPP was ignored. The specific procedural differences between the approach of Fung et al. [1987] and the present study are outlined in Heimann and Keeling [this volume].

Although Heimann and Keeling [this volume] have shown that the present method of estimating NPP results in annual integrals which are comparable to those established by Fung et al. [1987], there nevertheless exist differences in the seasonal patterns of biospheric CO_2 uptake and release between the two studies. These arise because of the higher spatial resolution employed by Fung et al. [1987], but also from the different functional forms of how the satellite data have been incorporated. If we calculate the GSNF by

evaluating the biospheric SNCT according to equation (3.1) with respect to the terrestrial biospheric fluxes for every grid box and then sum over the entire globe, we obtain 11.2 GtC (8.6 GtC in the northern and 2.6 GtC in the southern hemisphere) compared to 9.3 GtC as quoted by Fung et al. [1987]. Tans et al. [1989, p. 5163], in comparison, estimated 6.2 to 7.5 GtC in the northern hemisphere north of 18°N. using a two-dimensional model while Pearman and Hyson [1986, p. 101], also with a two-dimensional model, estimated 6.0 GtC in the northern hemisphere and 1.6 GtC in the southern hemisphere. Thus our estimates are somewhat higher than estimates by these other investigators.

An alternative approach to simulating seasonal changes in atmospheric CO_2 has been described by Gillette and Box [1986]. These authors derived the seasonal biospheric CO_2 exchange fluxes by means of a comprehensive biospheric process model, driven by climatic variables. The resulting seasonal variation of NPP and of the net biospheric fluxes is quite different than the pattern established in the present study, as may be appreciated by comparing our Figure 3, Panels (a) and (c), with Figure 3, curves (b) and (a), respectively, of Gillette and Box [1986]. (Note the different units and an error in their labeling of figures.) Based on the net carbon flux data for each 10° latitude band published by these authors, we calculate a SNCT of 4.8 GtC for the latitudes north of 20°N., 3.9 GtC between 0° and 20° N., 4.2 GtC between 0° and 20°S. and 0.9 GtC south of 20°S. Compared to the present study (see Table 3) the largest differences are present in the tropics of the northern hemisphere where Gillette and Box [1986] deduced a substantial seasonal flux approaching almost 80 percent of the SNCT in the extratropical regions. The reasons for these differences are not clear; it is possible that the satellite data which we have used may be contaminated by persistent cloud cover in the tropics [Fung et al., 1987], but also that the process model of Gillette and Box [1986] includes other factors which have been neglected in the present approach, such as the influence of moisture on soil respiration. It may be, therefore, that the presently deduced seasonal CO_2 fluxes in this zone represent only a zeroth order approximation to reality. Nevertheless, our simulation using these fluxes results in rather satisfactory predicted seasonal cycles at the (albeit few) tropical monitoring stations. A detailed comparison of the seasonal CO_2 fluxes deduced in the present study with the results of the biospheric model of Gillette and Box [1986] would be worthwhile but has not yet been undertaken.

Finally, we remark that the presently established annual cycle of the net biospheric CO_2 fluxes, on zonal average, varies in the northern hemisphere in a pattern resembling rather closely the simple source functions constructed by Azevedo [1982], which were subsequently used by Fung et al. [1983] in their original atmospheric CO_2 modeling study. This is readily apparent by comparing, for example, the time variation in Figure 3, Panel (c) at 50°N.

Fig. 3. Zonally averaged fluxes of the unperturbed terrestrial biosphere as a function of latitude and time and in the same flux units as Figure 1.   Panel (a). Net primary productivity for the same time period as Figure 1. The contour interval is 10 gC month^{-1} m^{-2} of land area. The solid line marks the latitude at which the midday sun reaches an elevation of 90°.   Panel (b). Heterotrophic respiration approximately for the year 1980 (see text). The contour interval is the same as in panel (a).   Panel (c). Net biospheric exchange flux, including biospheric fertilization and destruction as well as net primary productivity and respiration, for the same time period as Figure 1. The contour interval is 5 gC month^{-1} m^{-2} of land area. Negative fluxes, i.e., fluxes into the biosphere, are indicated by dashed contour lines in all three panels. Also, the first 6 months are displayed twice to reveal the annual cycle more clearly.

and 30°N. with Azevedo's high and low latitude curves, respectively. The major difference, however, is found in the tropical latitudes, where Azevedo assumed no time variation in the net flux in contrast to the present study.

3.3   Exchanges of CO_2 with the Surface Ocean

The exchange flux of CO_2 gas between the air and the sea, described by Heimann and Keeling [this volume], is modeled in the present study with a bulk formula, i.e., by an exchange coefficient multiplied by the difference in partial pressure of CO_2 (ΔpCO_2) in the surface layer of the sea ($pCO_{2\,sea}$) and the overlying air ($pCO_{2\,air}$). The exchange coefficient is assumed to be constant in time and space; its value was chosen to correspond to an atmospheric residence time of CO_2 with respect to the ocean of 7.87 years, equivalent to a gas exchange rate of 19.1 mol m^{-2} yr^{-1} at an atmospheric CO_2 mixing ratio of 290 ppm, consistent with Keeling et al. [this volume, a].

The seasonal variation of $pCO_{2\,sea}$ was calculated as a thermodynamic function of the monthly mean climatological sea-surface temperature fields. This results in a maximal air-sea CO_2 flux in early autumn, when sea surface temperatures are highest. In high latitudes the seasonal activity of the marine biosphere and the seasonally changing depth of the mixed layer opposes the temperature driven effect on $pCO_{2\,sea}$. Consequently, we reduced the temperature driven $pCO_{2\,sea}$ variation linearly to zero in the latitude zone between approximately 35° to 51° in each hemisphere and suppressed any seasonality entirely poleward of 51°. Also, the temperature driven variation in the coastal upwelling areas off the western coasts of Africa and South America was reduced to the variation calculated in the subtropical gyres 20° longitude further offshore.

In addition to the seasonally varying exchange flux, as described above, a mean annual disequilibrium between air and sea is imposed in the model. This disequilibrium is assumed to transfer globally 2.2237×10^{12} kgC yr^{-1} from the atmosphere into the ocean, as inferred from the global carbon cycle compartment model for the average of 1979–1980. Furthermore, a globally balanced pattern of large distinct source and sink regions was assumed in which the magnitudes of these sources and sinks were subject to two adjustable global parameters. We have determined the magnitudes of these parameters for 1980 by a fit, as described by Heimann and Keeling [this volume], to data of the mean annual atmospheric CO_2 concentration at a series of stations along a meridional section in the central Pacific Ocean [see Tables 1 and 2 of Keeling et al., this volume, b]. The influence of this oceanic source/sink pattern upon the seasonal cycle of atmospheric CO_2 is small, except in the tropical regions where the seasonally changing circulation induces time varying fluctuations, as described below in section 5.

Figure 4 displays a map of the peak-to-peak changes of the seasonal variation in the assumed oceanic $pCO_{2\,sea}$. Figure 5 summarizes the zonally averaged sea-air difference, ΔpCO_2, as a function of latitude and time of the year. The equatorial belt between approximately 10°S. and 10°N. exhibits excess $pCO_{2\,sea}$ values relative to the atmosphere throughout the year with little seasonal dependence. In the temperate latitudes during most of the year $pCO_{2\,sea}$ is smaller than in the overlying air, thus representing sink regions on annual average.

The SNCT with the ocean results in 0.64×10^{12} kgC in the northern and to 0.83×10^{12} kgC in the southern hemisphere. A comparison with the corresponding SNCT associated with the terrestrial biosphere reveals that the seasonality of the ocean plays a minor role in the northern hemisphere whereas in the southern hemisphere it is of comparable importance (see Table 3).
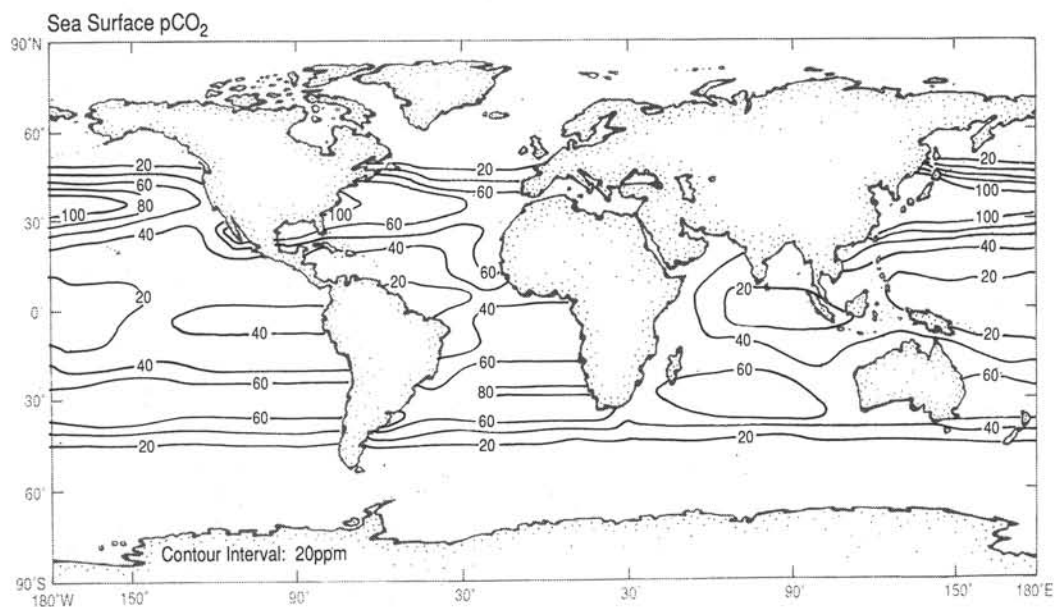

Fig. 4. Annual range, peak-to-peak, of the assumed variation in CO_2 partial pressure, pCO_{2sea}, in ppm, in the surface layer of the ocean.
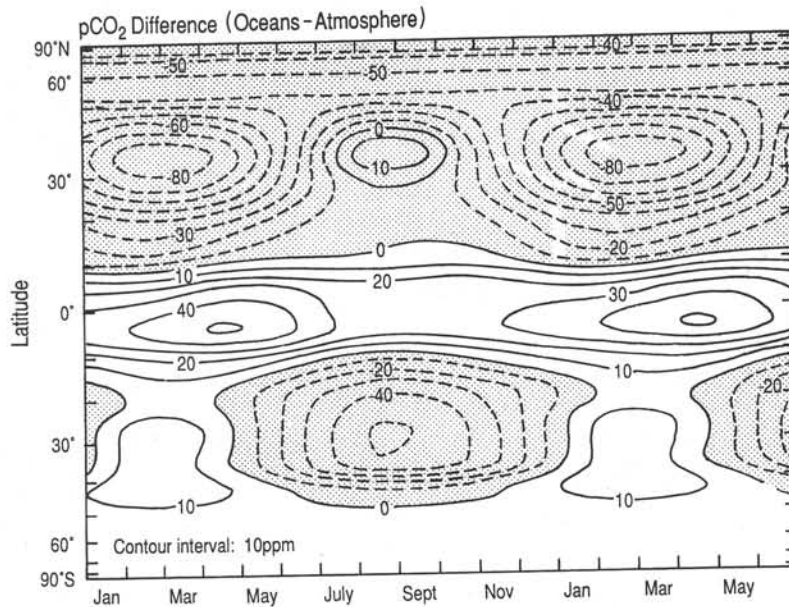
Fig. 5. Zonally averaged CO_2 partial pressure difference, ΔpCO_2, in ppm, between the ocean and the atmosphere displayed as a function of latitude and time. Dashed contour lines indicate negative flux, i.e. into the ocean.

3.4 The Industrial CO_2 Source

According to Rotty [1987], the release of industrial CO_2 from fossil fuel combustion and cement production varies seasonally to a minor extent. Rotty's estimate of CO_2 emissions for the year 1980 was used to implement the model source term [Heimann and Keeling, this volume]. The SNCT of fossil fuel is found to be only 0.06×10^{12} kgC in the southern and 0.18×10^{12} kgC in the northern hemisphere. Compared to the other two source components discussed above in subsections 3.2 and 3.3, the industrial CO_2 seasonal source variation is evidently negligible. The main influence of industrial CO_2 on the seasonal cycle is due to seasonally changing transport patterns as described below in section 5.

3.5 The Composite CO_2 Source

The zonally averaged sum of all CO_2 flux components is displayed in Figure 6 as a function of latitude and time. It is qualitatively similar to Figure 3, except in the southern hemisphere which is not dominated by the terrestrial biosphere. Note also that Figure 6 displays fluxes per unit area, whereas Figure 3 displays fluxes per unit of land area.

The annually averaged sum of all CO_2 fluxes on the resolution of the model grid is shown in Figure 7. The global picture is dominated by the large localized fossil fuel CO_2 release regions in the more industrialized countries in the northern hemisphere: United States of America, western and eastern Europe, China, and Japan. In addition southeastern Asia constitutes a modest source region owing to deforestation and changes in land use. The oceanic source-sink distribution is dominated by the outgassing region in the equatorial tropics and the large scale sink regions in temperate latitudes and foremost in the North Atlantic.

4. Observational Data

Atmospheric CO_2 data from several sources are compared in the present paper to the model simulation results. All station data have been decomposed into a seasonal cycle and a trend function, the latter consisting of an exponential and a spline function.

Data obtained by the Scripps Institution of Oceanography (SIO) have been described by Keeling et al. [this volume, a]. In addition we obtained atmospheric CO_2 data based on flask samples from the station network operated by the National Oceanographic and Atmospheric Administration (NOAA) This data set, which we obtained from The Carbon Dioxide Information Center at Oak Ridge, Tennessee, is described in detail by Komhyr et al. [1985]. We processed the NOAA flask data through the same analyzing scheme as the SIO data, in order to separate the seasonal cycle from the slowly varying trend.

Additionally, the Upper Atmosphere Research Laboratory in Sendai, Japan, provided us with data on the seasonal cycle measured by aircraft at five height levels in the troposphere over Japan [Tanaka et al., 1987a], and at the Antarctic research station, Syowa [Tanaka et al., 1987b]. These data consisted of two harmonics for each location.

5. Model Results

5.1 Time Decomposition Strategy

The model was run with each of the different source components for 4 model years. Each run was started from an initial uniform zero concentration field. The daily concentrations $C_i(\mathbf{x},t)$ of the 4th model year for each source component i, expressed relative to the mean annual model surface concentration at the South Pole,
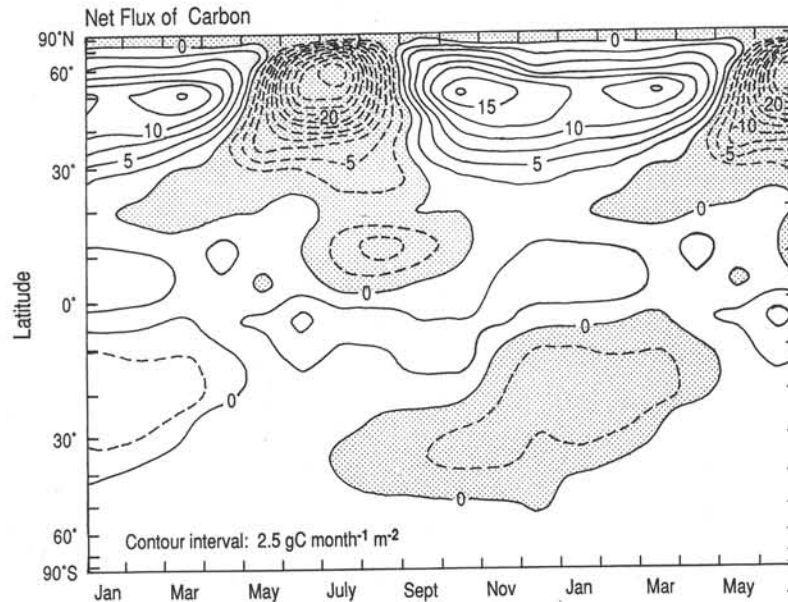
Net Flux of Carbon

Fig. 6. Zonally averaged net flux of carbon at the earth's surface, in the same units as Figure 1, displayed as a function of latitude and time. The contour interval is 2.5 gC month^{-1} m^{-2}. Dashed contour lines indicate negative fluxes, i.e. out of the atmosphere.

were added together [Heimann and Keeling, this volume, equation (4.2)] to form a composite concentration field

$$C_{CMPS}(\mathbf{x},t) = C_o + \sum_{i=1}^{n} C_i(\mathbf{x},t) \qquad (5.1)$$

The value of the constant C_o, representing the mean annual surface concentration at the South Pole, was chosen from a fit of the mean

annual model results to atmospheric CO$_2$ data [Keeling et al., this volume, a].

As an example, Figure 8 shows daily CO$_2$ concentration variation predicted by the model as a function of time at the La Jolla observing site (33°N., 117°W.). Different time scales of variation are clearly discernible. Hence for the purpose of analyzing and discussing the model results the composite concentration field

Annual Net Source Fluxes
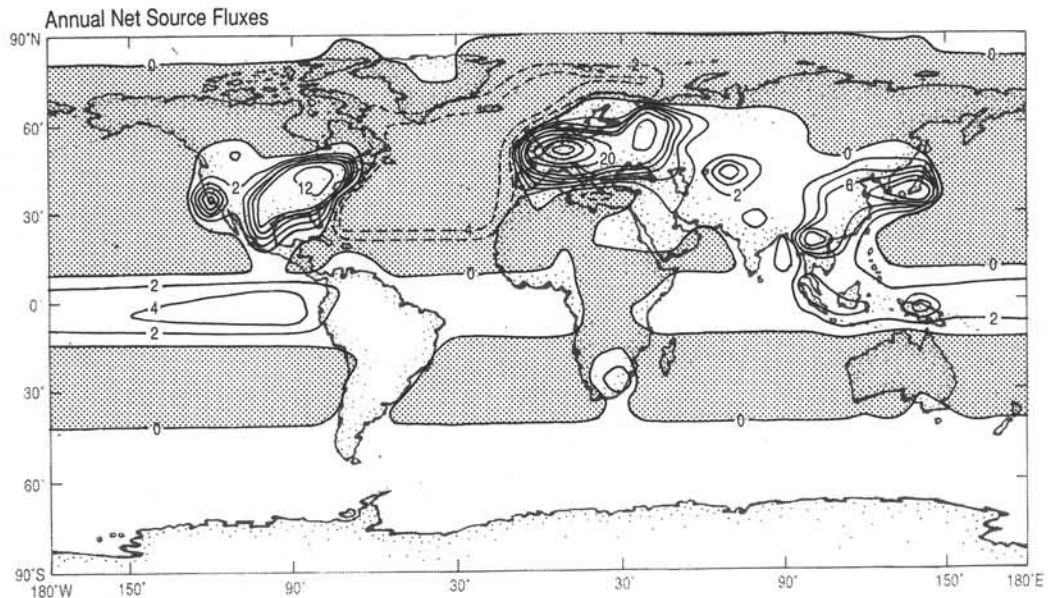
Fig. 7. Annually averaged net fluxes of CO$_2$ at the earth's surface as resolved on the model grid, in the same units as Figure 1. The contour interval is 2×10^{-2} kgC m^{-2} yr^{-1}.
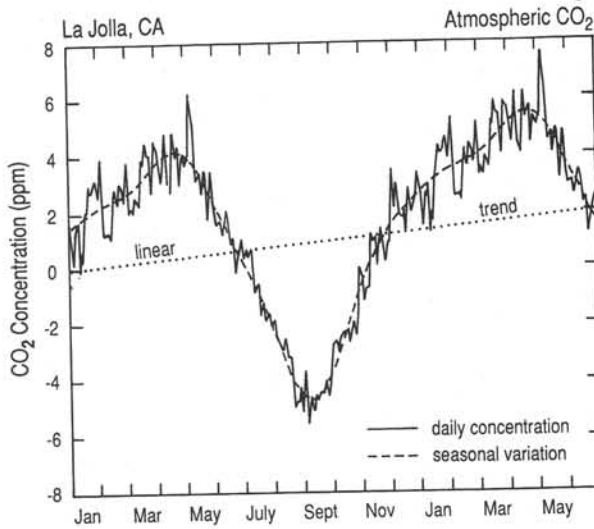
Fig. 8. Model predicted atmospheric CO_2 concentration, in ppm, as a function of time at station LJO (La Jolla, California, 33°N., 117°W.). Both daily concentration values and the seasonal variation, represented by 4 harmonics of the base period of 1 year, are shown. A linear trend, $a_t t$, is also plotted. The curves have been shifted such that the linear trend function vanishes on the first of January of the first year plotted.

$C_{CMPS}(\mathbf{x},t)$ at any location $\mathbf{x}$ and time t was subsequently decomposed into four parts

$$C_{CMPS}(\mathbf{x},t) = C_o + a_t t + C_{mean}(\mathbf{x}) +$$
$$C_{seas}(\mathbf{x},t) + C_{syn}(\mathbf{x},t) \qquad (5.2)$$

The decomposition includes, besides the constant term C_o,

(1) a linear trend in time representing a concentration increase, a_t, which, according to the quasi-stationary assumption applied to the year 1980, approaches the same value of $a_t = 1.32$ ppm yr^{-1} everywhere;

(2) a time-independent mean annual concentration field, $C_{mean}(\mathbf{x})$ expressed relative to C_o,

(3) a seasonal variation, $C_{seas}(\mathbf{x},t)$, expressed as the sum of the first four harmonics of a base period of 1 year;

(4) the remaining synoptic scale variability, $C_{syn}(\mathbf{x},t)$, reflecting variations on time scales from days to a few weeks.

Specifically, this separation was achieved by selecting, from the output of the model computation at every grid point, the corresponding time series of daily concentrations. These time series were subsequently detrended and Fourier transformed in order to obtain the coefficients of the first four harmonics constituting the seasonal variation at every grid point.

The distinction between the seasonal scale, C_{seas}, and the synoptic scale, C_{syn}, of variation was made because all sources and sinks were specified on a monthly basis and in the simulation were smoothly interpolated in time using Hermite cubics [de Boor, 1978, p. 52]. Hence any variability on time scales less than a month reflects primarily the effects of individual synoptic scale events as represented in the GWE wind fields used in the model. Accordingly, our data analysis procedure [Keeling et al., this

volume, a] evaluates the seasonal variation at the different monitoring sites directly in terms of four harmonics.

This paper will be entirely concerned with the terms $C_{seas}(\mathbf{x},t)$; and $C_{syn}(\mathbf{x},t)$; the discussion of the resulting mean annual field $C_{mean}(\mathbf{x})$ is deferred to the article by Keeling et al. [this volume, b].

5.2 Comparison of the Simulated Seasonal Variation with Station and Aircraft Data

In order to compare the CO_2 concentration variations at an observing station to the concentrations calculated by the model, the station location with respect to the model grid has to be specified. Special attention is needed in defining the vertical coordinate in the case of high mountain stations, since a fixed station elevation cannot be unambiguously translated into the model's vertical reduced pressure (sigma) coordinate system. This comes about because the coarse horizontal resolution of the model does not resolve individual mountain ranges. Thus the elevation of a station relative to the model topography has to be determined, which is then transformed into sigma coordinates by means of a standard atmosphere appropriate to the latitude of the station. Except when noted otherwise, we did not interpolate within the model grid, but selected the values at the nearest grid point in order to obtain the model concentration corresponding to a particular station location.

An additional complication arises when model results are compared to a station which is located close to local sources of CO_2. In order to obtain estimates of the CO_2 concentration of so-called "background air" selective sampling and data screening are used in the observing programs of the different CO_2 monitoring agencies. However, it is difficult to assess the amount of contamination still present in the observations. On the other hand, the model simulates calm, stagnant weather situations, which in the case of the fossil fuel source, for example, tend to increase the local CO_2 concentration. Thus a dilemma exists between identifying local contamination, which is not resolved in the model, and a possible sampling bias that underestimates the large scale average degree of contamination at the site. This problem is especially severe in the case of the mean annual concentration, where gradients of a few tenths of a ppm imply relatively large mean fluxes. It probably also impacts the comparison of model simulations and observations of the seasonal cycle of CO_2, especially at the La Jolla station (LJO).

In Figure 9 we compare the model predictions with observations obtained by the Scripps Institution of Oceanography (SIO) at the four low elevation northern hemisphere stations that were used to calibrate the respiratory flux of the terrestrial biosphere, as described above in subsection 3.2. The amplitude, as expected from the fitting procedure, but also the phase and shape of the modeled seasonal signal, generally agree with the observations, although the prediction misses the exact occurrence of the maximum and minimum concentration by a few weeks. Consistently the model predicted concentration starts to decrease too early, as compared to the data. Except for station PTB (Point Barrow, Alaska) the simulated minimum occurs too late, giving rise to a less rapid concentration drawdown in the model than is observed. This problem might be tied to the specification of the sources being only on a monthly basis, but it probably involves other defects in the model as well.
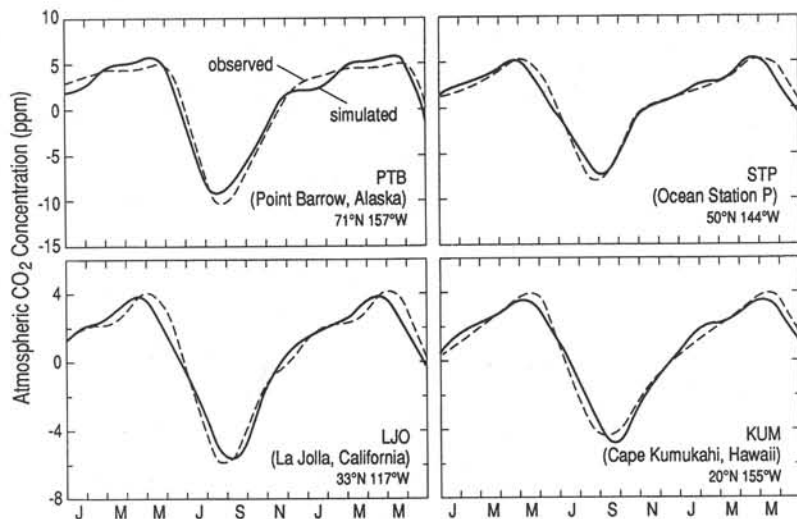
Fig. 9. Simulated seasonal variation of atmospheric CO_2, in ppm, compared to the observed variation at northern hemisphere stations PTB, STP, LJO, and KUM. Model and observational concentrations are represented by a sum of four harmonics fitted to the daily model prediction and to the individual observational data, respectively. The first 6 months are displayed twice in order to reveal the annual cycles more clearly. The data from these four stations were used to determine the free global parameter in the formulation of the biospheric respiration (see section 3.2 and Table 2).

Figure 10 displays model results obtained by the National Oceanic and Atmospheric Administration (NOAA) at four northern hemisphere stations that were not included in the set used to calibrate the model and, hence, provide an independent test of the performance of the model in the northern hemisphere. Additionally, Figure 11 displays the results obtained by SIO at the mountain station MLO (Mauna Loa Observatory, Hawaii, at 3397 m) and by

NOAA at the mountain station NWR (Niwot Ridge, Colorado, at 3749 m). The agreement, on average, is less good than for the stations used to calibrate the respiratory flux, but still satisfactory, especially for stations MLO and NWR.

The adopted modeling strategy permits a detailed investigation of the contribution of each of the different source components to the combined seasonal variation. This is exemplified in Figure 12,
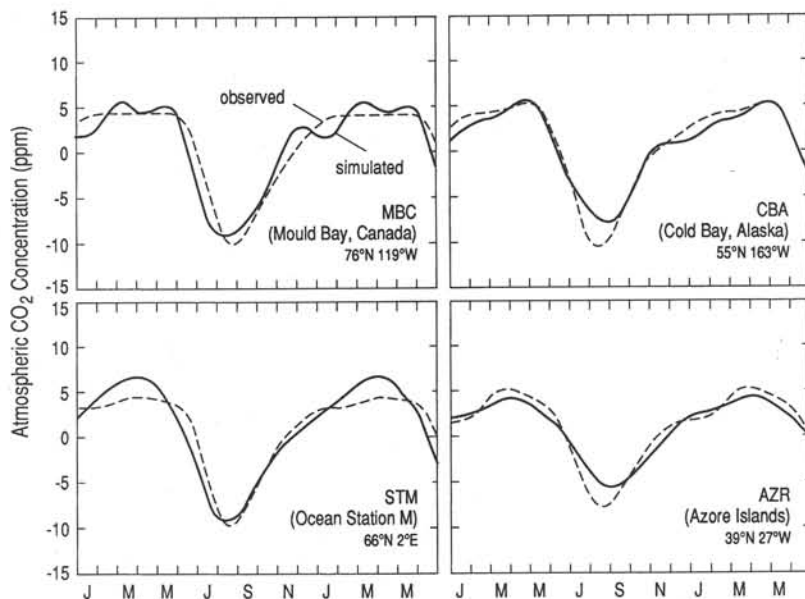

Fig. 10. Simulated seasonal variation of atmospheric CO_2, in ppm, compared to the observed variation at northern hemisphere stations MBC, CBA, STM, and AZR.
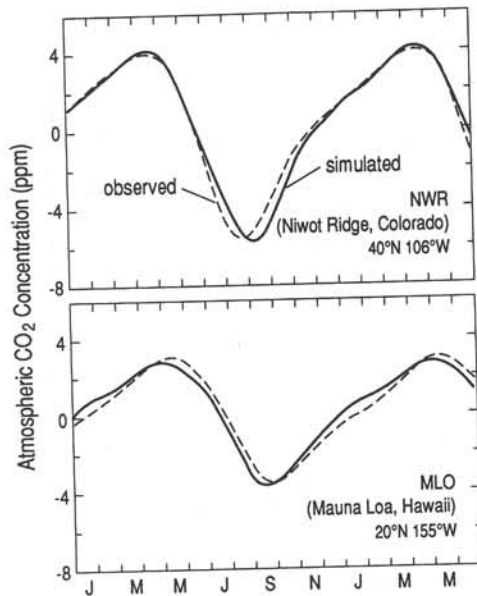
Fig. 11. Simulated seasonal variation of atmospheric CO_2, in ppm, compared to the observed variation at two mountain stations: NWR and MLO.

Fig. 12. Composite seasonal concentration variation of atmospheric CO_2 (shown as a solid line), in ppm, as predicted by the model for stations LJO and MLO together with its constituents: the variation resulting from the industrial CO_2 source, from the oceanic sources and sinks, and from the terrestrial biospheric source components. Seasonal variations derived from observations by SIO are also shown for comparison.

which shows composite signals generated by the model at stations LJO (La Jolla, California) and MLO (Mauna Loa, Hawaii) together with a decomposition of each of these signals into three constituents: contributions owing to the industrial CO_2 source, to the combined oceanic sources, and to the terrestrial biospheric sources. Clearly, the latter dominates the composite signal, a feature common to all extratropical locations in the northern hemisphere. The oceanic contribution is seen to oppose the biospheric signal.

The industrial CO_2 signal is small, nevertheless it is of the same order of magnitude as the oceanic contribution. This, in view of the relative strength of the seasonality in these two source components (cf. Table 3), is at first sight surprising; it results primarily from the seasonally changing transport patterns as they are represented in the model. In summer, the industrial CO_2 released at the ground over the continents is diluted into a greater volume of air, because the enhanced vertical convection over the continents mixes the troposphere more thoroughly. This results then in lower surface concentrations in summer as compared to winter.

Mauna Loa Observatory, being located near 20°N., also experiences changes in the atmospheric circulation associated with the annual changes of the strength and location of the Hadley cells, described in greater detail by Keeling et al. [this volume, b]. However, the present simulation results in a contribution of only 0.2 ppm from the the industrial CO_2 component to the total amplitude at Mauna Loa. This is considerably less than the 0.7 ppm variation found by Heimann et al. [1986]. In the latter study the authors simulated the transport of CO_2 by means of wind fields generated by the GISS climate model [Hansen et al., 1983]. These wind fields exhibit a Hadley cell extending further north than observed during the GWE period of 1978–1979.

Model results and observations for stations in the tropical latitude belt are presented in Figure 13. The observations are by SIO except for station SEY (Seychelles Islands) for which observations
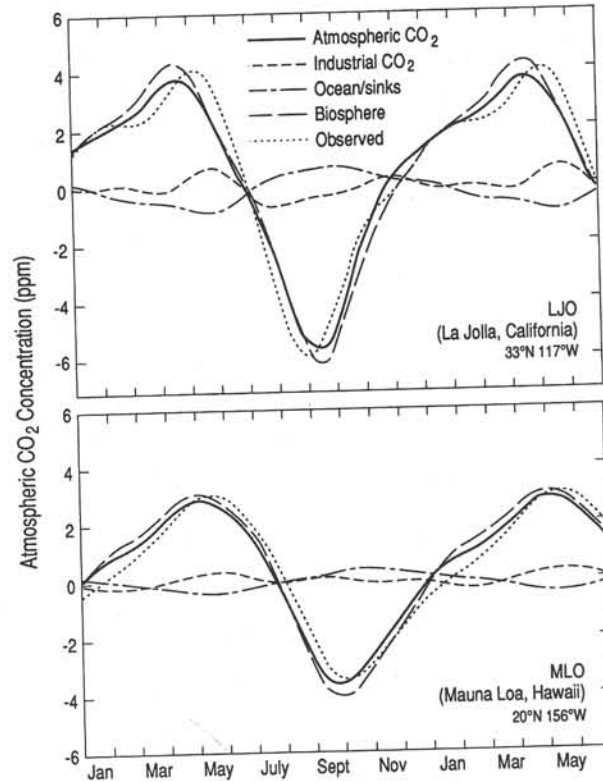
by NOAA are presented. The agreement of the model with observations is surprisingly good. These stations are, in general, far away from strong seasonal sources, hence their seasonal signal is strongly influenced by transport characteristics of the atmospheric circulation. This is exemplified by the occurrence of the maximum concentration at the Indian Ocean station SEY in March when air masses from the northern hemisphere carried by the winter monsoon circulation reach the location of the station.

Figure 14 displays for stations SEY and FAN (Fanning Island) the decomposition of the model generated signal into its individual constituents. At station SEY the industrial CO_2 contribution manifests itself in a pulse of air which is enriched in CO_2 by about 2 ppm. This pulse lasts from January through March. The terrestrial biospheric contribution by itself would cause maximum concentrations in July through October, contrary to the observations. Also at station FAN (Figure 14) industrial CO_2 contributes substantially to the resulting seasonal signal. Here, CO_2 enriched air from the northern hemisphere reaches the site in March through May, somewhat later than at station SEY in the Indian Ocean. It is thus almost in phase with the biospheric signal. The oceanic contribution is seen to oppose, and therefore partially cancel, the effect of industrial CO_2. This peculiar phasing affects the relationship
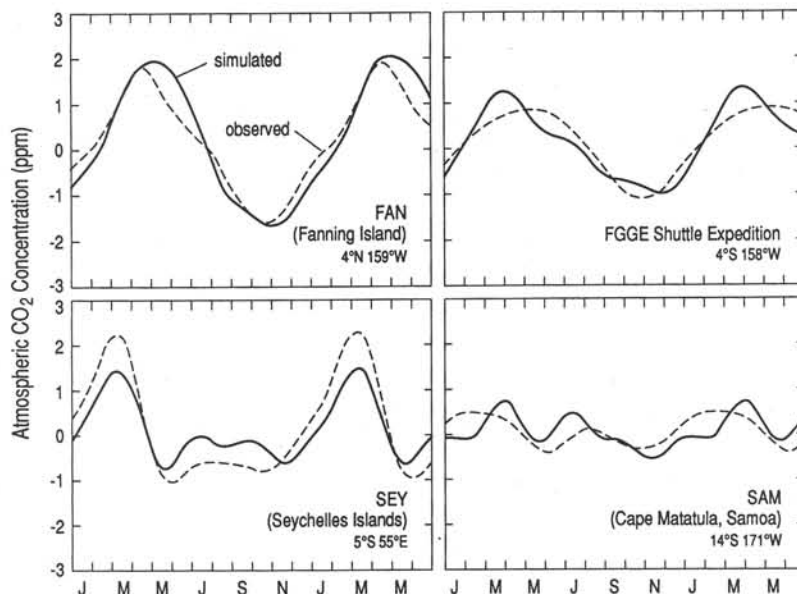
Fig. 13. Simulated seasonal variation of atmospheric CO$_2$, in ppm, compared to the observed variation at tropical stations FAN, FGGE (4°S.), SEY, and SAM.
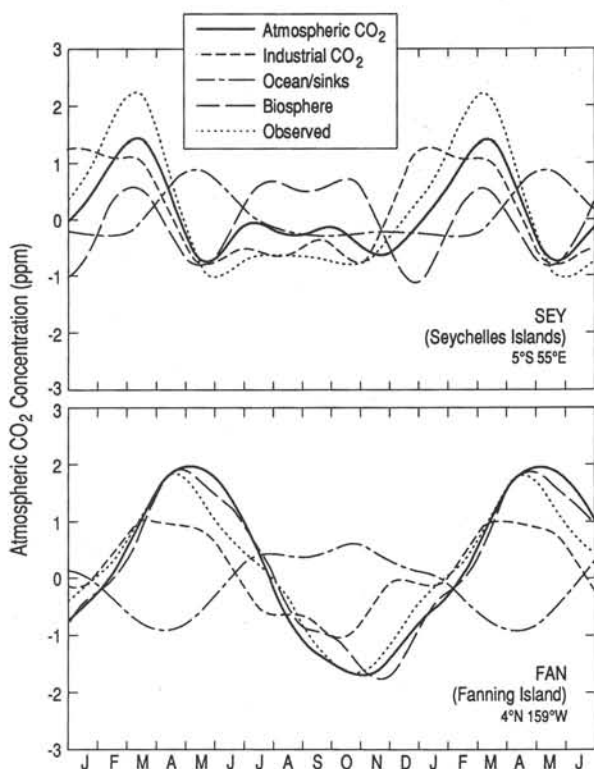

Fig. 14. Same as Figure 12, but for Indian Ocean station SEY and tropical Pacific station FAN. Seasonal variations derived from observations by NOAA at the Seychelles Islands and by SIO at Fanning Island are also shown for comparison.

between the isotopic ratio, $^{13}C/^{12}C$, and the concentration at this site, as discussed below.

Model results and observations for southern hemisphere stations are presented in Figure 15. The observations for station AMS (Amsterdam Island) are by NOAA, for station NZD (Baring Head, New Zealand) by Manning (private communication, see Keeling et al. [this volume], Appendix A), for station SYO (Syowa) by Tanaka et al. [1988], and for station SPO (South Pole) by SIO. The model only slightly overestimates the amplitude of the seasonal variation at stations SPO and SYO, but over estimates it by almost 100 percent at stations NZD and AMS. Also, there is also a significant phase difference of 4 weeks between model prediction and observations at Antarctic coastal station SYO. This poor agreement appears to be a common problem in modeling studies of atmospheric CO$_2$ in the southern hemisphere [see, for example, Pearman and Hyson, 1986].

Figure 16 displays the decomposition of the model generated signal for stations SPO and NZD. It is seen that the model predicts for the terrestrial biospheric contribution at the South Pole a variation of 1.9 ppm, peak-to-peak. This signal, larger than the composite signal, is opposed by the oceanic contribution, thus reducing the resulting variation to 1.3 ppm. Industrial CO$_2$ produces a variation of only 0.3 ppm. This latter signal is almost out of phase compared to the composite signal. The decomposition for station NZD is similar.

The vertical attenuation of the seasonal variation over Honshu Island, Japan at 35°N., together with observations from aircraft samples by Tanaka et al. [1985], is displayed in Figure 17. Shown are the amplitude, peak-to-peak, and time of the occurrence of the maximum and minimum concentration. For this comparison only the first and second harmonic of the seasonal variation have been used, as only those were available from the Japanese data analysis.
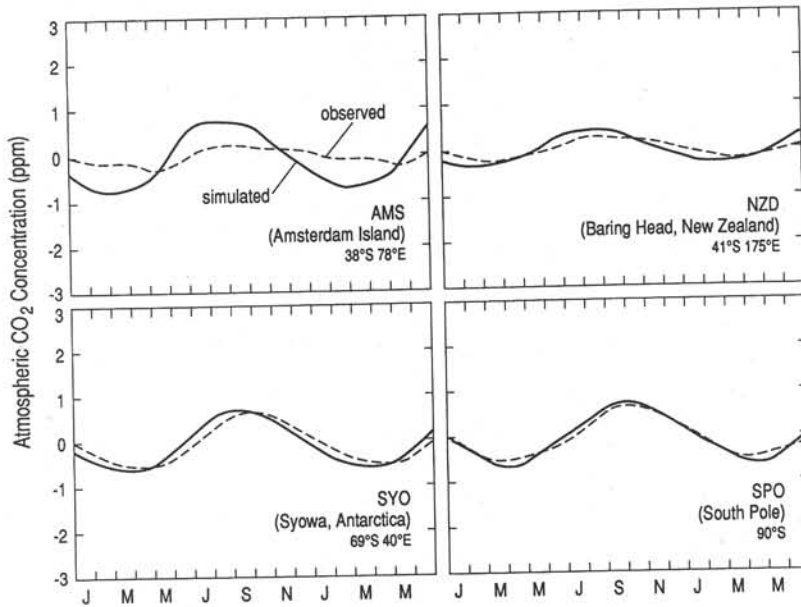
Fig. 15. Simulated seasonal variation of atmospheric CO_2, in ppm, compared to the observed variations at southern hemisphere stations AMS, NZD, SYO, and SPO.
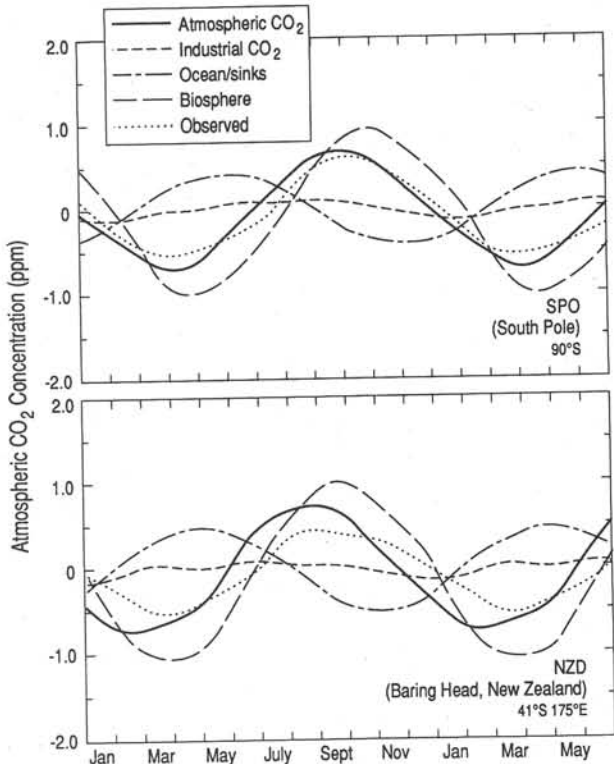

Fig. 16. Same as Figure 12, but for southern hemisphere stations NZD and SPO. Seasonal variations derived from observations by SIO are also shown for comparison.

The model portrays the attenuation of the amplitude with height rather satisfactorily; only below 2 km does the model underestimate the amplitude significantly. This reflects two limitations of the present transport model: there is no explicit boundary layer formulation and the rather coarse horizontal grid of approximately 8° by 10° cannot closely resolve the conditions over Japan. The
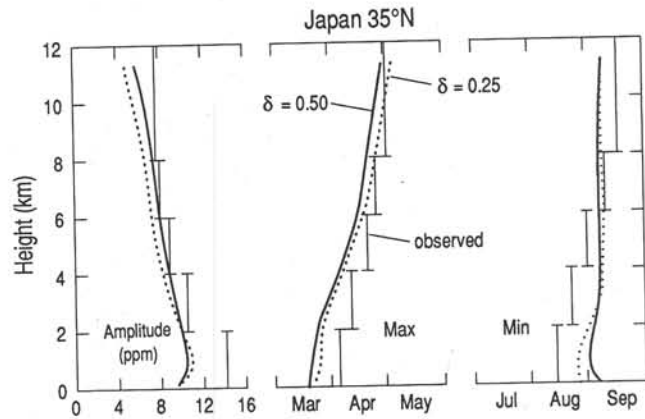

Fig. 17. Amplitude, peak-to-peak, in ppm, and times of maximum and minimum of the seasonal variation of atmospheric CO_2, in the vertical column over Japan at 35°N. Model results are shown both for the standard case and for the model prediction with the vertical convective parameterization reduced by a factor of 2 with respect to the standard case (see section 5.3). Also shown for comparison are observations of Tanaka et al. [1985].
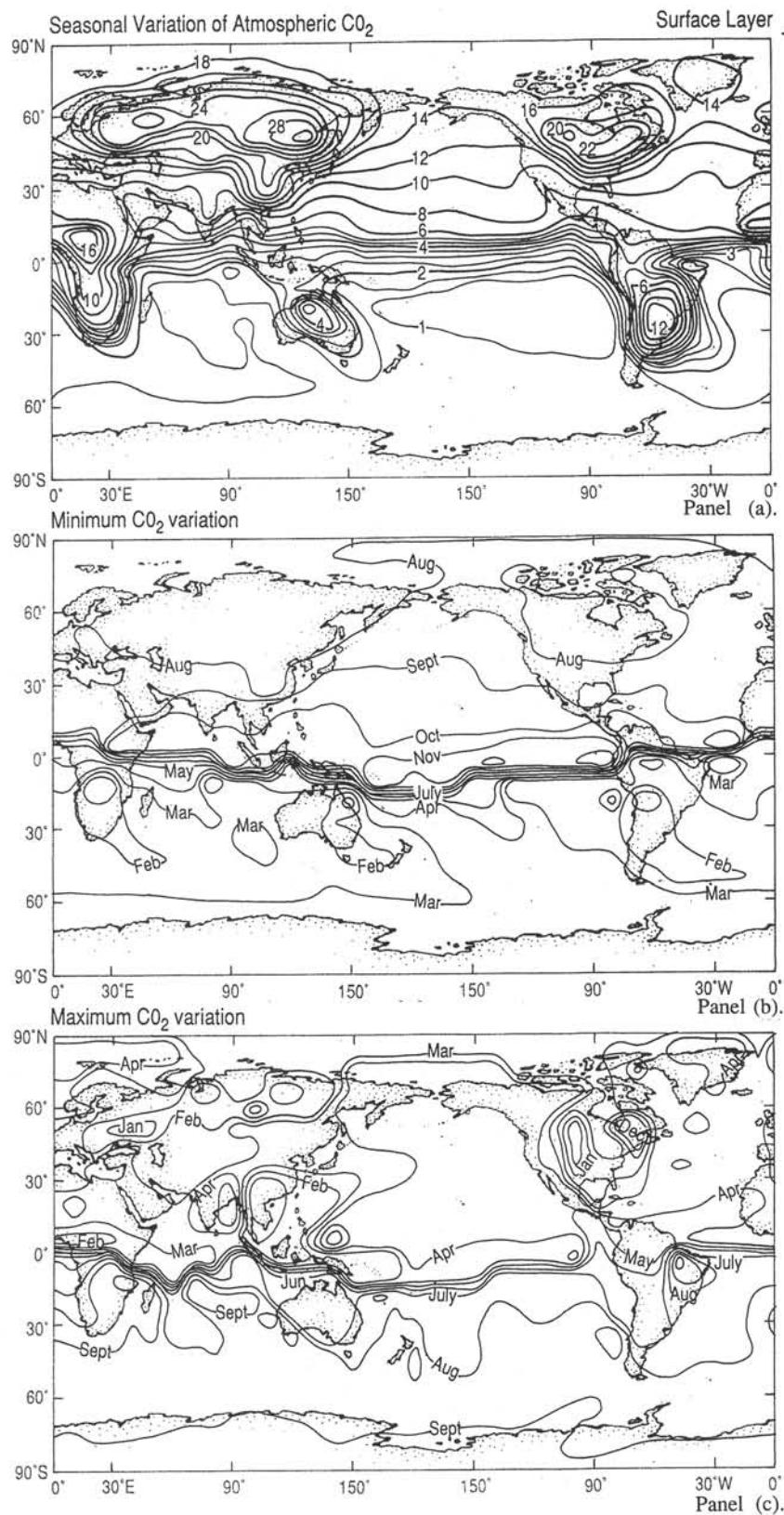
Fig. 18. Contour maps of the predicted seasonal variation of atmospheric CO_2 in the lowest model layer.
Panel (a). Amplitude, peak-to-peak, in ppm. Contour interval from 1 to 6 ppm is 0.5 ppm; above 6 ppm it is 2 ppm.   Panel (b). Time of the minimum.   Panel (c). Time of the maximum. Labelled isolines of (b) and (c) denote the middle of the corresponding month.

delay of the maximum with height is well represented in the model, although it lags the observations systematically by about 2 weeks. On the other hand the minimum concentration predicted by the model displays almost no delay with height, contrary to the observations. The cause of this phenomenon is not known.

5.3 Global Characteristics of the Seasonal Variation

The global distribution of the amplitude, peak-to-peak, of the seasonal variation predicted by the model in the surface layer of the atmosphere is presented in Panel (a) of Figure 18. Panel (b) displays the occurrence of the minimum and Panel (c) the occurrence of the maximum.

Large amplitudes exist over the northern hemisphere continents, as first seen in the CO_2 modeling study of Fung et al. [1983]. There are also large amplitudes over Africa in the tropical region, reflecting the seasonality of the local terrestrial biosphere (see Figure 2). The seasonal variation over the oceans in the southern hemisphere is rather small (less than 2 ppm) except eastward of the continents and south of 35°S., where the predominant westerly winds tend to propagate the terrestrial biospheric signal out over the open oceans.

In many respects Panel (a) of Figure 18 closely resembles the corresponding surface layer amplitude map published by Fung et al. [1987]. The apparent major difference is that their results exhibit regions of maximal seasonal amplitudes over the northernmost parts of the northern hemisphere boreal forests (for example, over southern Alaska, northern European USSR, and far north-eastern Siberia) which are absent or displaced toward the south in Figure 18, Panel (a). These differences of the amplitude patterns between the two studies primarily reflect differences in the representations of the biospheric source. There are two principal factors that tend to reduce our predicted seasonal fluxes in the high latitudes compared to the representation employed by Fung et al. [1987].

Firstly, solar radiation is explicitly included as a factor in prescribing NPP; secondly, the calculation of heterotrophic respiration allows a non-zero, albeit small, flux at monthly mean-surface air temperatures below −10°C. These factors might also be responsible for the somewhat better model simulation of the seasonal cycles in terms of phase and shape at the northern hemisphere stations as compared to the results of Fung et al. [1987, Figure 6].

According to the present model simulation, the timing of the minimum CO_2 (Figure 18, Panel (b)) displays a progressive delay of the order of 2 months, going from temperate latitudes of the northern hemisphere continents towards the tropical regions. South of the equator a sharp phase transition exists, delineating the northern hemisphere signal from the southern hemisphere signal. There is again a delay of about 1.5 to 2 months, between the occurrence of the minimum over the southern hemisphere continents and the arrival of the signal at the South Pole.

The timing of the maximum CO_2 of the seasonal variation (Figure 18, Panel (c)) mirrors the timing of the minimum, except that it appears more irregular in the northern hemisphere, particularly over the continents. As witnessed by station MBC (Mould Bay, Canada, see Figure 10) the signal displays a rather flat maximum during the winter season, when the respiratory flux from the surface is suppressed by low surface temperatures. Small local differences in the surface flux therefore give rise to rather large shifts in the occurrence of the maximum. Over the Indian Ocean and southeastern Asia the influence of the monsoon circulation may be seen. Over southeastern Asia the maximum occurs early in January, resulting from advection of CO_2 enriched air from the eastern Asian region. Likewise the maximum in March south of the equator in the western Indian Ocean reflects the winter monsoon circulation, as noted above in discussing the station SEY (Seychelles Islands, see Figure 13).

Figures 19 and 20 display model predicted amplitudes at two levels well above the boundary layer: in the lower troposphere
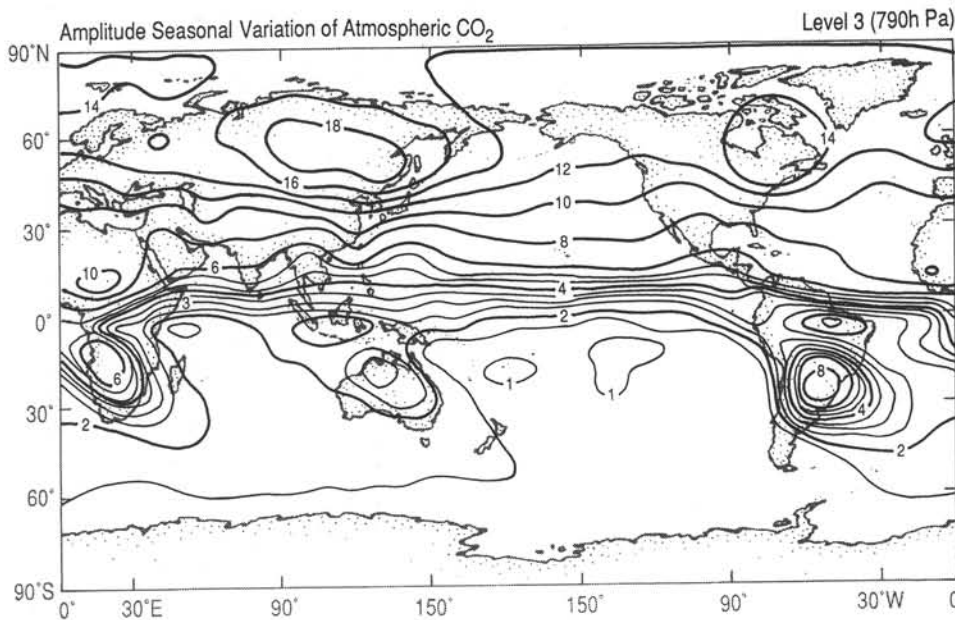

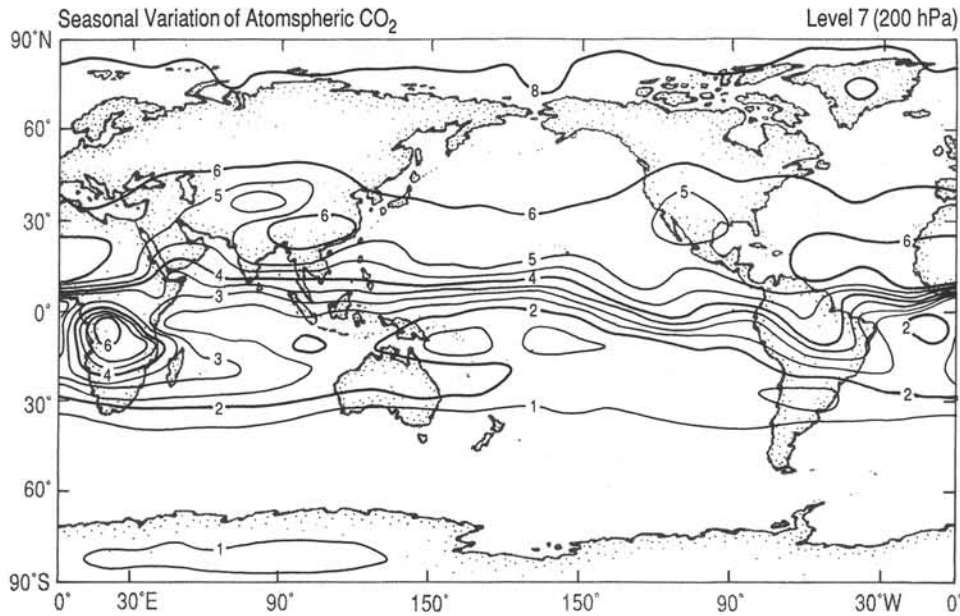Fig. 19. Same as Figure 18, Panel (a), but for third model layer located at about 790 hPa.

Fig. 20. Same as Figure 18, Panel (a), but for seventh model layer, located at about 200 hPa.

close to 790 hPa and in the upper troposphere close to 200 hPa, respectively. In the lower troposphere, the seasonal variation is similar to the signal at the surface, although somewhat smoothed. Over the Indian and Pacific Oceans in the southern hemisphere the signal increases slightly with height as has been observed in aircraft data near Australia [Pearman and Beardsmore, 1984]. In the upper troposphere the amplitude of the seasonal variation exhibits a maximum in the arctic region and a prominent secondary maximum south of the equator over the African continent. The latter is a consequence of the intense vertical convection coupled with the moderate seasonal source at the ground in central Africa.

The vertical structure of the seasonal variation generated by the model in the African and Indian Ocean region may more readily be seen in Figure 21, showing latitude-height cross sections of the peak-to-peak amplitude at 30°E. and at 60°E., respectively. The maximum in relative amplitude over Africa between 20°S. and the equator in the upper troposphere is clearly discernible in Panel (a) of Figure 21. This signal is propagated south of 20°S. over the Indian Ocean as seen in Figure 21, Panel (b). Here the signal at the surface (1.5 ppm) is considerably smaller than aloft (less than 2.5 ppm). Figure 21 also displays the steep attenuation of the signal in the northern hemisphere above 200 hPa, where the tropopause, on average, is located.

Figure 22 displays the ratio of the amplitude of the seasonal variation near the middle of the atmosphere at model level 5 (approximately 470 hPa) and at the surface. Stippled areas display regions where the amplitude increases with height, which is the case over most of the southern hemisphere oceans, most notably around 20°S. where the amplitude at 470 hPa is more than double the amplitude at the surface, which, however, is rather small in these areas (see Figure 18, Panel (a)). Figure 22 may be directly compared with Figure 10, Panel A in Fung et al. [1987], displaying the same feature. Both model results are very similar, except for a few details, which result because our simulation includes the effects of

other sources as well as the terrestrial biosphere, and because our transport model employs a coarser horizontal resolution than the model used in the study by Fung et al. [1987].

The attenuation of the seasonal cycle as a function of height is dependent on the chosen strength of the vertical convective parameterization in the transport model. In Figure 17, where we display amplitude and phase of the seasonal signal in the vertical column over Japan also for the model case with the reduced vertical convection (dashed lines), referred to in section 2, it is seen that the amplitude decreases slightly more with height than in the standard case. The times of occurrence of the maximum and the minimum are hardly affected by changing this model feature, however. This behaviour is typical; the case with the reduced vertical convection exhibits an amplitude decrease with height which in the northern hemisphere is approximately 20 percent larger than the decrease in the standard case. In the southern hemisphere this effect is reversed: a reduction of the vertical convection increases the seasonal amplitudes in the upper troposphere.

5.4 ^{13}C – ^{12}C Interrelationships

Further insight into the seasonal variation of atmospheric CO$_2$ may be obtained by looking at its stable carbon isotope ratio. The latter we express by the commonly used reduced isotopic ratio δ defined as

$$^{13}\delta = r/r_s - 1 \qquad (5.3)$$

where r and r_s denote the ^{13}C/^{12}C ratio of the sample and of a standard, respectively (see equation 5.3 in Heimann and Keeling [this volume]). Henceforth we omit the left subscript 13 on δ as do Heimann and Keeling [this volume].

To compute the distribution of the reduced ratio of atmospheric carbon dioxide by means of the three-dimensional transport model we specified for each of the different carbon sources and sinks their
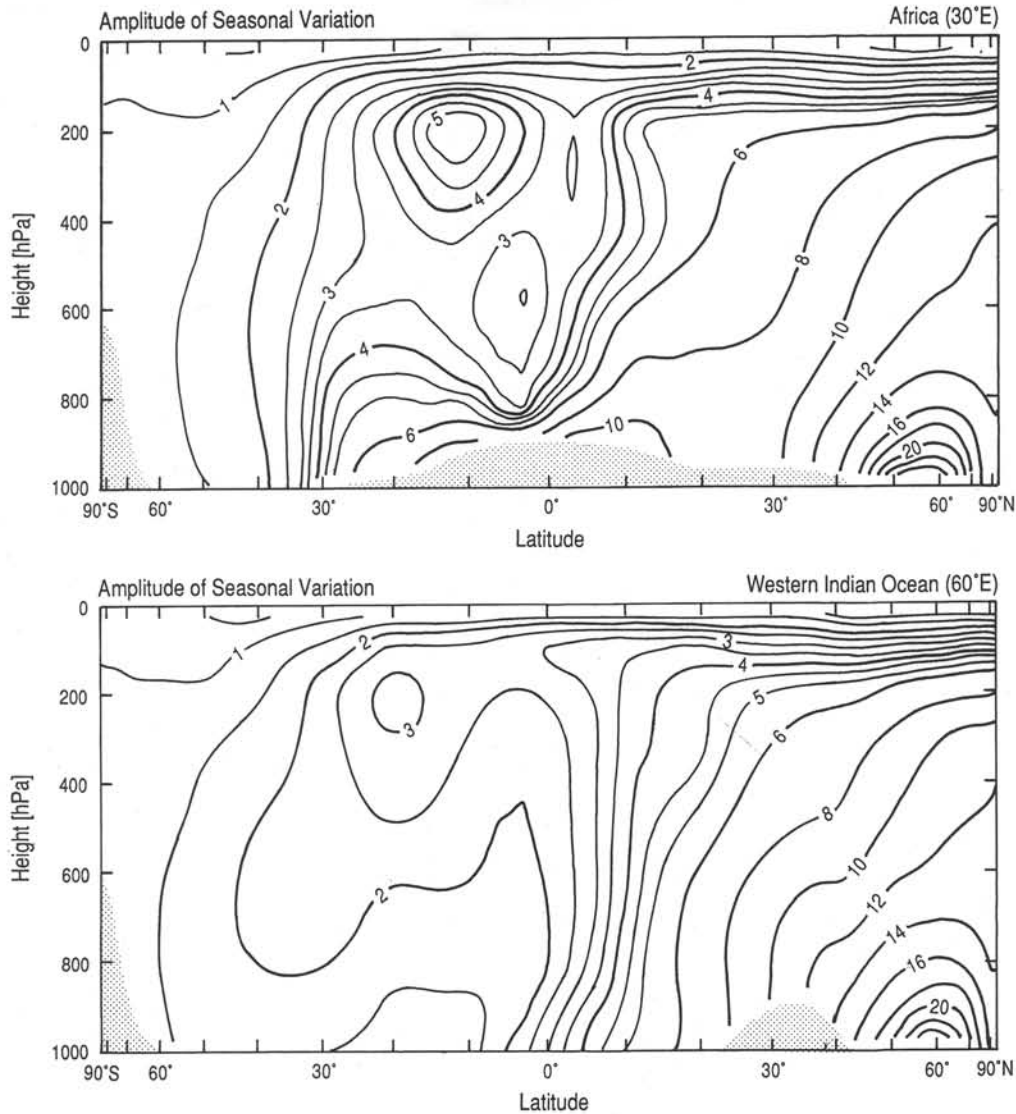
Amplitude of Seasonal Variation   Africa (30°E)

Amplitude of Seasonal Variation   Western Indian Ocean (60°E)

Fig. 21. Model predicted amplitude, peak-to-peak, of the seasonal variation of atmospheric CO_2, in ppm, in two meridional-vertical cross sections.   Panel (a). At 30°E. over Africa.   Panel (b). At 60°E. over the western Indian Ocean. Contour interval from 0 to 5 ppm is 0.5 ppm; above 5 ppm it is 2 ppm.

isotopic ratio. The procedure that was used is described in detail by Heimann and Keeling [this volume]. The composite isotopic ratio field was obtained by the superposition of 11 components, 10 of which were computed directly from their corresponding CO_2 components by multiplication with an appropriate isotopic ratio factor. The additional component, arising from the temperature dependent fractionation between gaseous CO_2 and dissolved inorganic carbon in the surface ocean, necessitated a separate model run.

The basic assumptions of the isotopic calculations [see Heimann and Keeling, this volume, section 5] were as follows:

(1) A constant isotopic ratio of industrial CO_2 ($\delta_{IND} = -27.28‰$).
(2) A constant and geographically uniform isotopic ratio of CO_2

fluxes to and from the terrestrial biosphere ($\delta_{PHO} = -25.53‰$, and $\delta_{RES} = -25.26‰$, respectively, [loc. cit., equations 5.20 and 5.23] for the period 1979–1980.

(3) A constant and geographically uniform isotopic composition of dissolved inorganic carbon in the surface ocean ($\delta_m = 1.6373‰$) [loc cit., Table 7], also for 1979–1980.

The model-derived isotopic field of atmospheric CO_2 was decomposed into four parts analogous to the CO_2 concentration fields (see equation 5.2 above). Only the seasonal variation, $\delta_{seas}(\mathbf{x},t)$, is discussed here. Synoptic variations are discussed briefly in subsection 5.5.

As expected, the isotopic fields generated by the model are dominated by the biospheric component, owing to the relatively large
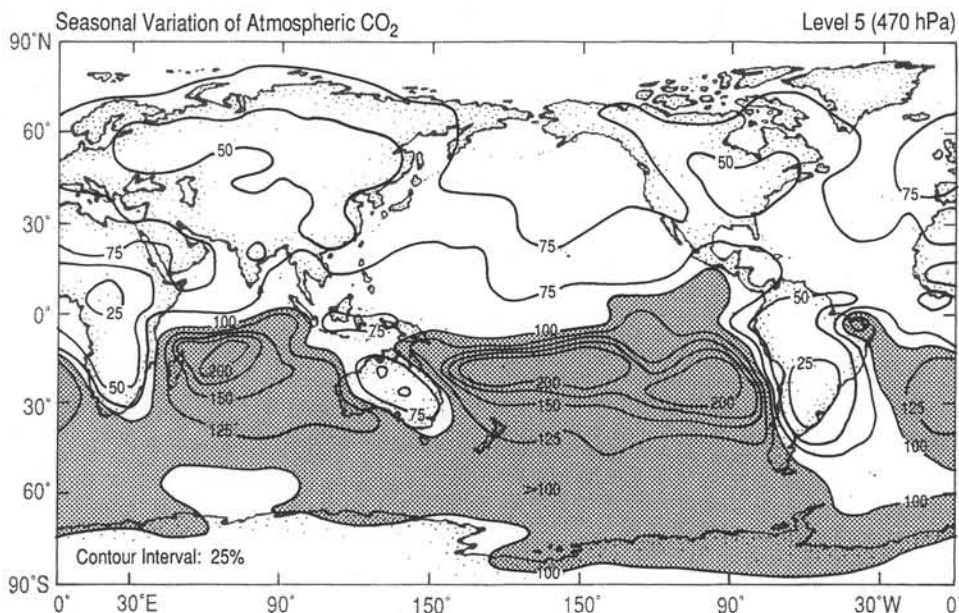
Fig. 22. Ratio of the amplitude of seasonal variation of atmospheric CO$_2$ at model level 5 (470 hPa) over the amplitude at the surface. Stippled regions exhibit values larger than 100 percent.

fractionation effect between the atmospheric CO$_2$ and the carbon of biospheric material. Nevertheless, the ocean plays a subtle role in the relationship between the reduced isotopic ratio, δ, and the CO$_2$ concentration.

Figure 23 displays model predictions of $\delta_{seas}(t)$ versus $C_{seas}(t)$ at three locations: PTB (Point Barrow, Alaska), FAN (Fanning Island) and SPO (South Pole). If CO$_2$ of biospheric origin were added or removed from the atmosphere, the corresponding points on the plots would remain on an approximately straight line with a slope of $-0.050‰$ ppm^{-1} [see equation 3.3 of Keeling et al., this volume, a]. This is seen to be almost the case at the northern hemisphere station PTB, where the terrestrial biospheric component dominates the predicted seasonal cycle. Nevertheless, the presence of oceanic components with hardly any isotopic signature leads to a hysteresis-type of relationship between δ_{seas} and C_{seas}, especially at low latitudes and in the southern hemisphere. Such a behaviour has been discussed in data analysis of atmospheric ^{13}C [Kamber, 1980; Friedli, 1983; Francey, 1985; Inoue and Sugimura, 1985] and more extensively in a modeling study by Pearman and Hyson [1986].

The exact form of the hysteresis curve is difficult to observe, in view of the required high measuring precision for δ and CO$_2$ as discussed in detail by Francey [1985]. We identify the following series of characteristics (in increasing order of complexity) in order to define quantitatively the δ versus C relationship:

(1) The apparent isotopic composition δ_I of the CO$_2$ added and removed to the atmosphere during a seasonal cycle.

(2) The appearance of a single loop or of a figure-eight, and the direction of movement on the curve.

(3) The spread of the curve, as measured, for example, by the concentration difference between those two points, in winter and summer, when the isotopic composition equals the annual average (i.e., when $\delta_{seas} = 0$).

The apparent isotopic composition, δ_I, is conveniently determined from a linear regression of δ_{seas} versus C_{seas}^{-1} (see equation (6) in Mook et al. [1983]). For small variations relative to the mean annual CO$_2$ concentration at the site, C_{a0}, the slope s of the $\delta_{seas}(t)$ versus $C_{seas}(t)$ relationship as displayed in Figure 23 corresponds to

$$s = \frac{\delta_I - \delta_{a0}}{C_{a0}} \qquad (5.4)$$

where δ_{a0} denotes the isotopic ratio corresponding to C_{a0}

Table 4 lists observed and model-calculated values of δ_I at the series of north-south trending locations. The model values have been computed by a regression analysis of daily model values of $\delta_{seas}(t) + \delta_{syn}(t)$ versus $(C_{seas}(t) + C_{syn}(t))^{-1}$ at each model grid point. An estimate of δ_I at each of the the station locations was subsequently obtained from the neighboring grid points by bilinear interpolation.

In the northern hemisphere the model displays the same trend of δ_I versus latitude as seen in the observed data. Starting out in the high northern latitudes with δ_I being close to the assumed isotopic composition of biospheric CO$_2$, δ_I gradually becomes more negative as the equatorial region is approached. According to the model, this behaviour results from an oceanic seasonal signal opposing the biospheric component. The former, on the order of 1 ppm peak to peak, increases slightly going southwards, while the latter decreases sharply, as may be seen by comparing Figure 12 for station LJO and Figure 14 for station FAN. South of the equator, both observed and model predicted values of δ_I become less negative. South of the tropical region, the model, as in the far north, predicts δ_I values which are close to those of biospheric carbon, or even more negative. A strongly negative value is predicted for the South Pole, but not confirmed by the data (see Table 4).

The model predicts throughout the temperate latitudes of each hemisphere a clockwise rotation along a hysteresis curve with a
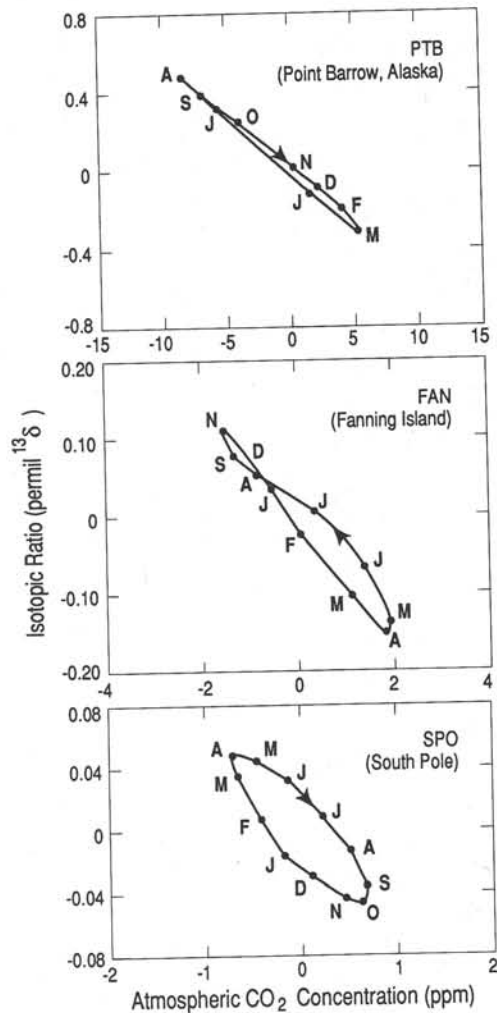
Fig. 23. Model predicted relationship between the seasonal component of reduced isotopic ratio $\delta(t)$ and concentration $C(t)$ of atmospheric CO_2 at three observing stations: PTB (upper panel), FAN (middle panel), and SPO (lower panel). The middle of each month is denoted by its first letter.

single loop as time moves through one full year. The relationship between δ_{seas} and C_{seas} becomes more complex in the tropical region as indicated for station FAN (Fanning Island) in Figure 23.

Comparing these hysteresis loops with those reported in the two-dimensional modeling study of Pearman and Hyson [1986], we notice that at both locations, PTB (Point Barrow) and at FAN (Fanning Island) their model predicts the same shape and rotation sense as depicted in Figure 23. However, at SPO (South Pole) Pearman and Hyson calculate a counterclockwise rotation, contrary to the present result. A fraction of this variance may be explained by our inclusion of the temperature-dependent isotopic fractionation in CO_2 of oceanic origin, an effect which was ignored in the study by Pearman and Hyson [1986].

A detailed comparison of the predicted direction of movement with the few available data sets has not yet been attempted. How-

ever, the data for station PTB (Point Barrow) shown by Keeling et al. [this volume, a, Figure 12] and of the aircraft measurements of Friedli [1983] over Switzerland indicate a counterclockwise rotation, contrary to the present model result. On the other hand the observations at Tsukuba, Japan, by Inoue and Sugimura [1985] display a clockwise rotation, although these measurements have been made close to local sources at the surface and may not truly reflect large scale conditions as simulated by the model. The analysis by Francey [1985] of the Cape Grim data also reveals clockwise rotation. If the counterclockwise rotation sense in the northern hemisphere were confirmed by more station data, then it would imply an oceanic component with a phase opposite to the one in the present model formulation.

The modeling of the δ_{seas} versus C_{seas} relationship represents a challenging task, whereby one attempts not only to assess correctly the seasonal cycle in concentration, but also the relative contribution of its major components as discriminated by their isotopic ratio. Further data on the isotopic composition of atmospheric CO_2 of the highest possible precision are needed.

5.5 Synoptic Scale Variations

The wind fields of the transport model resolve a large fraction of air movements on the synoptic scale. Hence the movement of air masses of different origins exhibiting contrasts in concentration is, at least partially, represented in the model. The simulated concentration at a particular station therefore exhibits fluctuations on time scales of days to a few weeks, termed synoptic scale variability, as shown in Figure 8.

As an example, Figure 24 displays the 700 hPa geopotential surface (dashed, thin contour lines) together with the simulated CO_2 concentration (solid thick contour lines) in model layer 4 (corresponding approximately to the height of the Mauna Loa Observatory: 3400 m) over the North Pacific Ocean on April 22, 1979, 00 hrs., universal time (UT). At this time of the year the terrestrial biosphere of the northern hemisphere begins, on net, to absorb CO_2. Continental air masses, however, still exhibit high concentrations of CO_2 as a result of CO_2 released during the previous winter season. A large cyclone centered over far eastern Siberia draws at its southern flank an air mass enriched in CO_2 out of the Asian continent. A subtropical anticyclone centered near 20°N., 170°E. blocks further southward movement of air in this region. Further to the east, however, along the eastern border of the anticyclone, CO_2 enriched air is moving southward in the direction of the Hawaiian Islands (indicated by the black circle in Figure 24). Consequently, the model predicts a rise in concentration at Mauna Loa station for the following days.

A second example is provided in Figure 25, displaying concentration in the surface layer of the model together with the geopotential of the 850 hPa level 10 days later on May 2, 00 UT. A cyclone located south of the Aleutian Islands in the eastern Pacific at its southern flank CO_2 directs enriched air toward Ocean Station P (50°N., 150°W., black circle in Figure 25), hence effecting a concentration rise during the following days at this site.

The short-term variations in CO_2 predicted by the model may be compared to observations of CO_2 obtained during the period December 1978–November 1979 of the GWE wind fields. Figures 26 and 27 display daily observations together with corresponding model predictions for 00 UT at the Mauna Loa Observatory and

TABLE 4. Apparent Isotopic Composition of CO$_2$ Added or Removed
from Atmosphere at Various Stations

Station Name	Approximate Latitude	δ_I(observed) (‰)	δ_I(model) (‰)
Point Barrow, Alaska (PTB)	71°N.	−25.1	−25.7
La Jolla, California (LJO)	33°N.	−28.3	−29.0
Cape Kumukahi, Hawaii (KUM)	20°N.	−26.6	−29.9
FGGE Shuttle Expedition	13.8°N.	−30.7	−31.0
	8°N.	−30.2	−31.7
	3°N.	−35.7	−30.7
	0°	−30.3	−26.0
	4°S.	−23.3	−19.9
	9.6°S.	−27.5	−13.8
	15.6°S.	−12.3	−18.0
Cape Grim, Tasmania (CGR)	41°S.	−22.3	−25.3
South Pole (SPO)	90°S.	−23.2	−29.7

Note

Source of data: Data at land stations PTB, LJO, KUM, and SPO are from Table 5 of Keeling et al. [this volume, a], at station CGR from Francey and Goodman [1985, p. 36], for FGGE Shuttle Expedition from Keeling et al. [1983, Table 8].

Ocean Station P. The two instants of time, which were discussed above with the synoptic maps, are indicated by vertical arrows. In order to display discrepancies between model and data only on synoptic time scales, the plotted model curve $C(t)|_{model}$ was constructed (cf. equation (2.4) of Keeling et al. [this volume, a]) using the observed seasonal cycle, $C_{obs\ seas}(t)$, and trend function, $C_{obs\ rem}(t)$, i.e.,

$$C(t)\Big|_{model} = (C_{obs\ rem}(t) + C_{obs\ seas}(t)) + C_{syn}(t)\Big|_{model} \qquad (5.5)$$
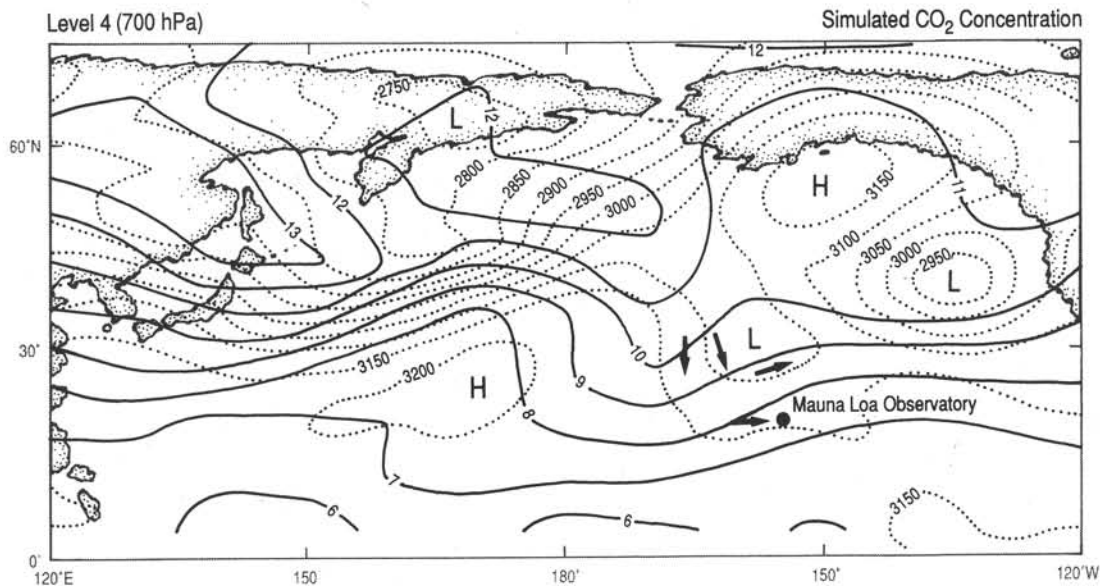

Fig. 24. Map showing the simulated CO$_2$ concentration, in ppm, in model layer 4 together with geopotential height of 700 hPa surface over the northern Pacific Ocean on April 22, 1979, 00 UT. Solid isolines: concentration, in ppm. A constant value of 330 ppm has been subtracted from the concentration field prior to plotting. Dashed isolines: geopotential height in m, contouring interval: 50 m. Letters L and H indicate locations of major cyclones and anticyclones, respectively. The black dot marks the location of the CO$_2$ observing station MLO (Mauna Loa Observatory, Hawaii). The arrows show the direction of airflow in the vicinity of the station.

Level 1 (850 hPa)   Simulated CO₂ Concentration
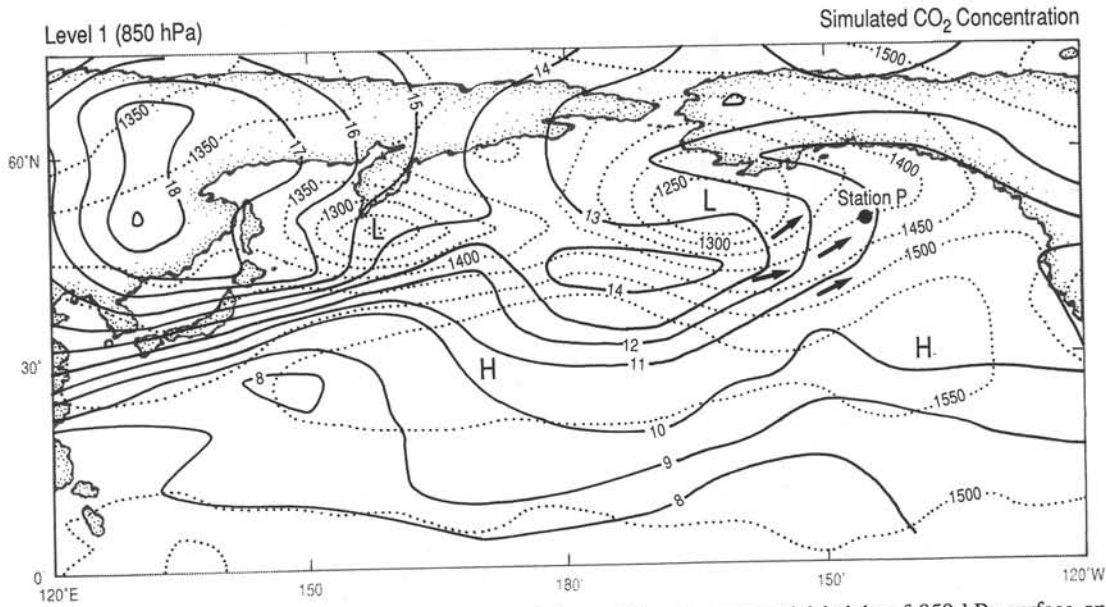

Fig. 25. Same as Figure 24, but for surface layer of the model and geopotential height of 850 hPa surface on April 29, 1979, 00 UT. The black point and the arrows mark the location and direction of airflow in the vicinity of the CO₂ observing station STP (Ocean Station P).

Thus the differences between model predictions and data, on the seasonal time scale as displayed in Figures 9 and 11, are not included in Figures 26 and 27.

The agreement is far from perfect, nevertheless quite a few of the observed fluctuations are matched in the model simulation. This is quite surprising in view of the coarse spatial resolution of

the present model, its lack of an explicit boundary layer formulation, and a subgridscale vertical convection held constant during each month.

A cross-correlation of model and data time series for the entire period December 1978 to November 1979 reveals a linear correlation coefficient of 0.49 for Mauna Loa (290 data points) and of
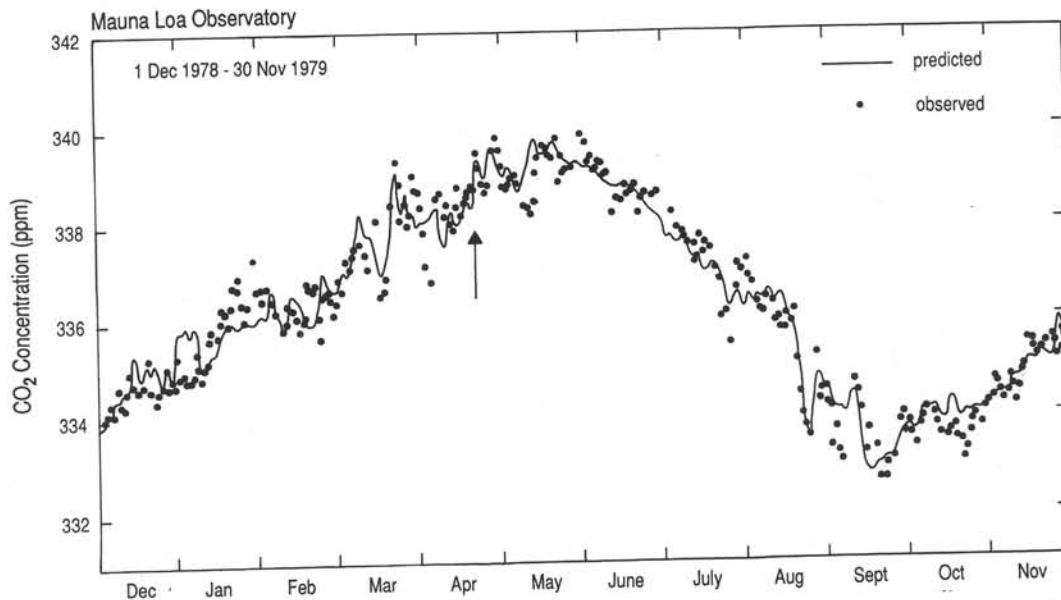

Fig. 26. Model predicted daily concentration at 00 UT (solid line) together with daily observations at Mauna Loa Observatory, Hawaii, for the time period December 1, 1978, to November 30, 1979. The arrow indicates the date of the synoptic map displayed in Figure 24.
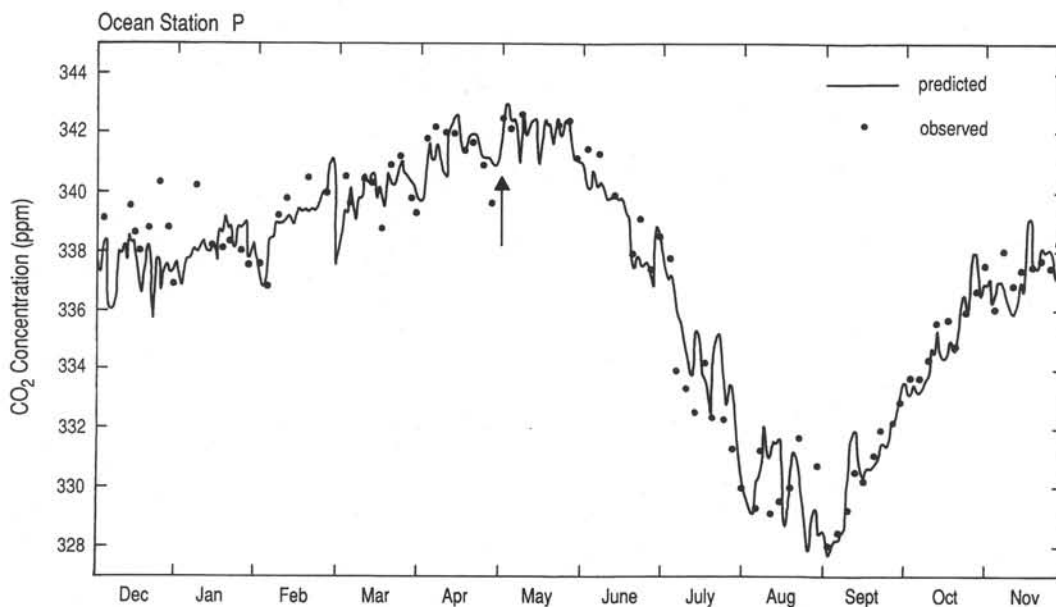
Fig. 27. Same as Figure 26, but for Ocean Station P. The arrow indicates the date of the synoptic map displayed in Figure 25.

0.55 at Ocean Station P (92 data points) for a time lag of 0 days, dropping to insignificant levels for time lags larger than about 2 days (see Figures 28 and 29). This statistical analysis was performed using only the synoptic scale variation of the observed and model-predicted time series. The effective number of degrees of freedom was estimated from the autocorrelation within each time series to be about 60 data points, making the linear correlation at lag 0 days significant at the 0.9999 level for the Mauna Loa and at the 0.99999 level for the Ocean Station P time series.

A summary of the statistical properties of the synoptic scale variation in concentration, C_{syn}, and also of the corresponding varia-

tion in the reduced isotopic ratio, δ_{syn}, at six selected stations is given in Table 5. Displayed are standard deviations of concentration, $\sigma(C_{syn})$ and of the reduced ratio, $\sigma(\delta_{syn})$, together with the correlation and the linear regression coefficient between δ_{syn} and C_{syn}. All properties were evaluated for the entire year from December 1978 to November 1979, and also for 3-month intervals.

As expected, the statistical properties vary substantially between the northern and the southern hemisphere stations. At Point Barrow (PTB) the synoptic scale variations are largely determined by air masses enriched or depleted by CO_2 of biospheric origin. This results in a linear correlation coefficient close to -1 between δ_{syn}
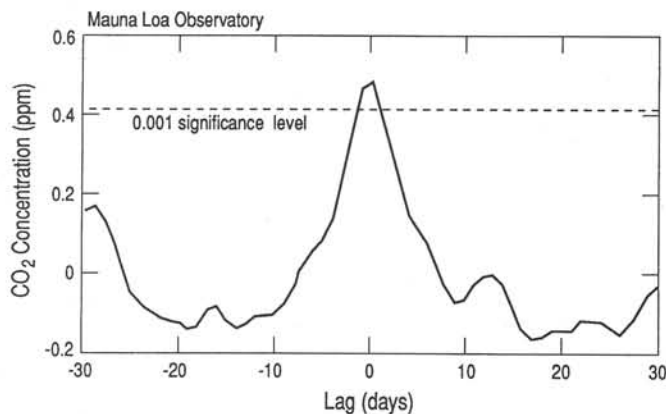

Fig. 28. Cross-correlation between model predicted and observed synoptic scale CO_2 concentration variation at Mauna Loa Observatory, Hawaii. The dashed line indicates the significance level of the linear correlation coefficient corresponding to a probability of the null hypothesis (no correlation) of 0.001.
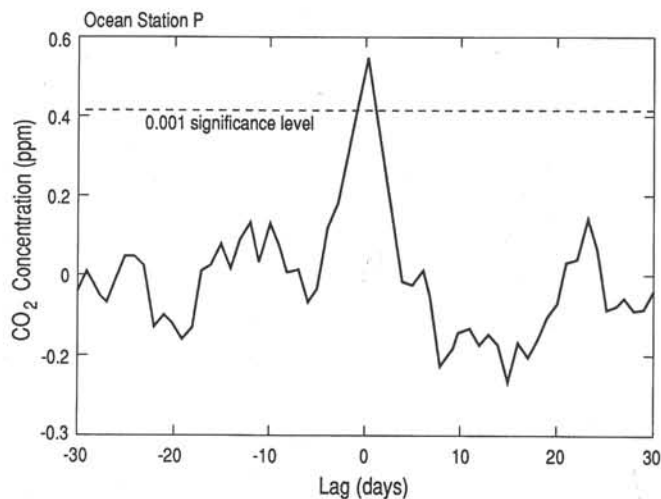

Fig. 29. Same as Figure 28, but for the Ocean Station P time series.

TABLE 5. Statistics of Model Generated Synoptic Scale Variation of Atmospheric
CO_2 Concentration, C_{syn} (in ppm) and Reduced Isotopic Ratio,
δ_{syn}, (in ‰) at Selected Stations

Season*	PTB	LJO	KUM	FAN	NZD	SPO
Sigma (C_{syn})						
DJF	0.7126	0.7886	0.5631	0.2565	0.1611	0.0387
MAM	0.6486	0.7693	0.6270	0.4302	0.1111	0.0298
JJA	1.3028	0.4336	0.2694	0.2224	0.1510	0.0525
SON	1.5932	0.5401	0.3647	0.3413	0.1588	0.0454
Full Year	1.1335	0.6497	0.4779	0.3228	0.1464	0.0424
Sigma (δ_{syn})						
DJF	0.0381	0.0539	0.0482	0.0343	0.0172	0.0048
MAM	0.0376	0.0556	0.0465	0.0445	0.0088	0.0033
JJA	0.0714	0.0220	0.0138	0.0204	0.0060	0.0034
SON	0.0814	0.0317	0.0205	0.0159	0.0106	0.0041
Full Year	0.0603	0.0432	0.0356	0.0309	0.0114	0.0039
Correlation Coefficient						
δ_{syn} vs C_{syn}						
DJF	−0.9949	−0.9859	−0.9805	−0.6555	−0.8627	−0.7236
MAM	−0.9755	−0.9788	−0.9821	−0.8990	0.1038	−0.1635
JJA	−0.9603	−0.9123	−0.8461	−0.6351	−0.7865	−0.7097
SON	−0.9910	−0.8859	−0.7947	−0.5863	−0.8858	−0.7596
Full Year	−0.9786	−0.9561	−0.9413	−0.7287	−0.6659	−0.6213
Constant B of Regression						
$\delta_{syn} = A + B\ C_{syn}$						
DJF	−0.0532	−0.0674	−0.0840	−0.0877	−0.0921	−0.0889
MAM	−0.0566	−0.0707	−0.0728	−0.0930	0.0082	−0.0180
JJA	−0.0526	−0.0464	−0.0434	−0.0582	−0.0311	−0.0463
SON	−0.0506	−0.0519	−0.0447	−0.0273	−0.0590	−0.0691
Full Year	−0.0520	−0.0635	−0.0700	−0.0698	−0.0517	−0.0576

*DJF refers to December through February, etc.

and C_{syn}. The linear regression coefficient results in approximately −0.05 ‰ ppm^{-1}, as expected.

In the southern hemisphere air masses of oceanic origin interfere with variations originating in continental air masses. At Baring Head, New Zealand (NZD), the standard deviation of C_{syn} is 0.15 ppm. If these synoptic scale variations were entirely caused by the passage of continental air masses over the station we would expect a corresponding standard deviation of the reduced ratio δ_{syn} to be a factor of 20 smaller. The model result shows, however, a standard deviation of 0.011‰ for the station, reflecting other sources of real variation or errors in sampling or analysis. Indeed, the temperature-dependent fractionation between gaseous CO_2 and dissolved inorganic carbon in the ocean produces source/sink patterns in the atmospheric $^{13}C/^{12}C$ ratio, because CO_2 emanating from waters that are colder than the global average exhibit a $^{13}C/^{12}C$ ratio lower than atmospheric values, and vice versa. Air masses which have been for some time over these regions acquire more negative δ values relative to the reduced ratio of background air. Therefore the passage of air masses originating in such areas will contribute to the variability in δ, but not in concentration. Correspondingly, the correlation between δ_{syn} and C_{syn} drops to smaller absolute values, as, for example, −0.67 at Baring Head, New Zealand (NZD).

Table 5 reveals also substantial seasonal variations in the statistical properties of C_{syn} and δ_{syn}. They reflect the complex seasonal variability in the passage of air masses different origin, being quite different from station to station.

The ability of the model to predict the synoptic scale of the concentration variations serves primarily two purposes:

(1) It provides a stringent test of the model together with its wind fields. On these short time scales both different parameterizations of subgridscale motions and errors show up markedly in the model response over the ocean or aloft.

(2) In analyzing atmospheric observations at a given station, model-calculated concentration variations using actual meteorological wind fields could provide an additional tool to discriminate between local contamination and long-range advection of CO_2 enriched air, thus helping to establish the concentration of so-called "background air" [Pearman et al., 1983].

6.   Conclusions

Our formulation of the carbon cycle with a three-dimensional model allows an almost satisfactory simulation of the seasonal cycle of the atmospheric CO_2 concentration as a function of latitude and time. Nevertheless, the in-depth comparison between model results and observations reveals several discrepancies tied in part to deficiencies in the three-dimensional transport model and in part to the specification of carbon sources and sinks.

In the northern hemisphere the seasonal cycle of CO_2 is essentially controlled by the seasonality of photosynthesis and respiration of land plants. The rather good agreement between model and data suggests that the simple model for plant growth by Kumar and Monteith [1981], in conjunction with data on insolation and, most notably, satellite data on the reflective properties of the plant canopy (vegetation index), provide a realistic estimate of net primary productivity. The cruder estimate of the respiratory fluxes from surface temperatures, adjusted by a global scale factor, appears to play a secondary role in the determination of the shape of the seasonal cycle of atmospheric CO_2.

In the tropical regions a substantial fraction of the seasonal signal is generated by industrial CO_2 and by oceanic CO_2 exchange, both of which are influenced by the seasonally changing tropical circulation of the atmosphere. The good agreement between model and data suggests that the tropical circulation is realistically portrayed.

The largest relative discrepancies between model and data exist in the southern hemisphere. According to the model calculation, the terrestrial biosphere and the oceans contribute opposing signals of the same order of magnitude. The resulting net signal is thus susceptible to small variations in either component. This circumstance may explain the rather large interannual changes in the seasonal cycle in terms of amplitude and phase, as have been documented, for example, by Keeling et al. [this volume, a] at the South Pole, and by Beardsmore and Pearman [1987] at Cape Grim Observatory.

The most important limitations of the present modeling effort are as follows:

(1) The meteorological wind fields are from a single year, approximately 1979, and, hence are not representative of a climatic average.

(2) The parameterization of subgridscale vertical exchange processes is kept constant during each month at every grid point.

(3) The model uses a rather coarse horizontal resolution of approximately 8° latitude by 10° longitude.

(4) Heterogeneous data have been used to construct the terrestrial biospheric source function: insolation has been estimated using satellite albedo data, and surface temperatures from the GWE data set, both for 1979; whereas the vegetation index data span the period from November 1983 to October 1984.

(5) The modeled oceanic CO_2 source component represents only a zeroth order approximation to reality. Indeed, effects associated with seasonal activities of the marine biota are very crudely portrayed; effects of a time and space-varying bulk coeffecient for gas exchange are ignored altogether.

Future modeling efforts should address these points. The present study demonstrates, in our opinion, that a realistic three-dimensional simulation of long lived atmospheric tracers based on archived global meteorological analyses is feasible. The simulation of the atmospheric CO_2 concentration and its isotopic ratio provides a valuable insight into the current state of the global carbon cycle.

References

Azevedo, A. E., Atmospheric distribution of CO_2 and its exchange with the biosphere and the oceans, Ph.D. thesis, Columbia University, New York, 1982.

Beardsmore, D. J., and Pearman, G. I., Atmospheric carbon dioxide measurements in the Australian region: data from surface observations, *Tellus*, v. 39B, p. 42–66, 1987.

de Boor, C., *A practical guide to splines*, 392 p., Springer-Verlag, New York, 1978.

Enting, I. G., and Mansbridge, J. V., Seasonal sources and sinks of atmospheric CO_2: Direct inversion of filtered data, *Tellus*, v. 41B, p. 111–126, 1989.

Francey, R. J., and Goodman, H. S., Systematic error in, and selection of, in-situ $\delta^{13}C$, in *Baseline 83–84*, publication of CSIRO/Division of Atmospheric Research, Australia, p. 27–36, 1985.

Friedli, H., Messung der Konzentration, des $\delta^{13}C$ und des ^{18}O von Kohlendioxyd an kleinen atmosphärischen Luftproben, Masters Thesis, University of Bern, Switzerland, 1983.

Fung, I. Y., Analysis of the seasonal and geographical patterns of atmospheric CO_2 distributions with a three-dimensional tracer model in *The Changing Carbon Cycle: A Global Analysis*, edited by J. R. Trabalka and D. E. Reichle, p. 459–473, Springer-Verlag, New York, 1986.

Fung, I. Y., Prentice, K., Matthews, E., Lerner, J., and Russell, G., Three-dimensional tracer model study of atmospheric CO_2: Response to seasonal exchanges with the terrestrial biosphere, *Journal of Geophysical Research*, v. 88, p. 1281–1294, 1983.

Fung, I. Y., Tucker, C. J., and Prentice, K. C., Application of advanced very high resolution radiometer vegetation index to study atmosphere-biosphere exchange of CO_2, *Journal of Geophysical Research*, v. 92, p. 2999–3015, 1987.

Gillette, D. A., and Box, E. O., Modeling seasonal changes of atmospheric carbon dioxide and carbon 13, *Journal of Geophysical Research*, v. 91, p. 5287–5304, 1986.

Hansen, J., Russel, G., Rind, D., Stone, P., Lacis, A., Lebedeff, S., Ruedy, R., and Travis, L., Efficient three-dimensional global models for climate studies: Models I and II, *Monthly Weather Review*, v. 111, p. 609–662, 1983.

Heimann, M., and Keeling, C. D., A three-dimensional model of atmospheric CO_2 transport based on observed winds: 2. Model description and simulated tracer experiments, in *Aspects of Climate Variability in the Pacific and the Western Americas*, edited by D. H. Peterson, this volume, American Geophysical Union, Washington, DC, 1989.

Heimann, M., Keeling, C. D., and Fung, I. Y., Simulating the atmospheric carbon dioxide distribution with a three-dimensional tracer model, in *The Changing Carbon Cycle: A Global Analysis*, edited by J.R. Trabalka and D.E. Reichle, p. 16–49, Springer-Verlag, New York, 1986.

Houghton, R. A., Boone, R. D., Fruci, J. R., Hobbie, J. E., Melillo, J. M., Palm, C. A., Peterson, B. J., Shaver, G. R., and Woodwell, G. M., The flux of carbon from terrestrial ecosystems to the atmosphere in 1980 due to changes in land use: Geographic distribution of the global flux, *Tellus*, v. 39B, p. 122–139, 1987.

Inoue, H., and Sugimura, Y., The carbon isotopic ratio of atmospheric carbon dioxide at Tsukuba, Japan, *Journal of Atmospheric Chemistry*, v. 2, p. 331–344, 1985.

Kamber, D., Modellierung der Variationen von CO_2 und $\delta^{13}C$ in Nord- und Südhemisphäre, Masters Thesis, University of Bern, Switzerland, 1980.

Keeling, C. D., Carter, A. F., and Mook, W. G., Seasonal latitudinal and secular variations in the abundance and isotopic ratios of atmospheric CO_2, 2. Results from oceanographic cruises in the tropical Pacific ocean, *Journal of Geophyhsical Research*, v. 89, p. 4615–4628, 1984.

Keeling, C. D., Bacastow, R. B., Carter, A. F., Piper, S. C., Whorf, T. P., Heimann, M., Mook, W. G., and Roeloffzen, H., A three dimensional model of atmospheric CO_2 transport based on observed winds: 1. Analysis of observational data, in *Aspects of Climate Variability in the Pacific and the Western Americas*, edited by D. H. Peterson, this volume, American Geophysical Union, Washington, DC, 1989a.

Keeling, C. D., Piper, S. C., and Heimann, M., A three dimensional model of atmospheric CO_2 transport based on observed winds: 4. Mean annual gradients and interannual variations, in *Aspects of Climate Variability in the Pacific and the Western Americas*, edited by D. H. Peterson, this volume, American Geophysical Union, Washington, DC, 1989b.

Komhyr, W. D., Gammon, R. H., Harris, T. B., and Waterman, L. S., Global atmospheric CO_2 distribution and variations from 1968–1982 NOAA/GMCC CO_2 flask sample data, *Journal of Geophysical Research*, v. 90, p. 5567–5598, 1985.

Kumar, M. and Monteith, J. L., Remote sensing of crop growth, in *Plants and the Daylight Spectrum*, edited by H. Smith, p. 133–144, Academic Press, New York, 1981.

Matthews, E., Global vegetation and land use: New high-resolution data bases for climate studies, *Journal of Climate Applied Meteorology*, v. 22, p. 474–478, 1983.

Mook, W. G., Koopmans, M., Carter, A. F., and Keeling, C. D., Seasonal, latitudinal and secular variations in the abundance and isotopic ratios of atmospheric carbon dioxide: 1. Results from land stations, *Journal of Geophysical Research*, v. 88, p. 10915–10933, 1983.

Pearman, G. I., and Beardsmore, D. J., Atmospheric carbon dioxide measurements in the Australian region: Ten years of aircraft data *Tellus*, v. 36B, p. 1–24, 1984.

Pearman, G.I. and Hyson, P., Activities of the global biosphere as reflected in atmospheric CO_2 records, *Journal of Geophysical Research*, v. 85, p. 4468–4474, 1980.

Pearman, G.I., and Hyson, P., Global transport and inter-reservoir exchange of carbon dioxide with particular reference to stable isotopic distributions, *Journal of Atmospheric Chemistry*, v. 4, p. 81–124, 1986.

Pearman, G. I., Hyson, P., and Fraser, P. J., The global distribution of atmospheric carbon dioxide: 1. Aspects of observations and modeling, *Journal of Geophysical Research*, v. 88, p. 3581–3590, 1983.

Rotty, R. M., Estimates of seasonal variation in fossil fuel CO_2 emissions, *Tellus*, v. 39B, p. 184–202, 1987.

Siegenthaler, U., and Münnich, K. O., $^{13}C/^{12}C$ fractionation during CO_2 transfer from air to sea, in *SCOPE 16: Carbon Cycle Modelling*, edited by B. Bolin, p. 249–258, John Wiley and Sons, Chichester, 1981.

Tanaka, M., Nakazawa, T., and Aoki, S., Seasonal and meridional variations of atmospheric carbon dioxide in the lower troposphere of the northern and southern hemispheres, *Tellus*, v. 39B, p. 29–41, 1987a.

Tanaka, M., Nakazawa, T., Shiobara, M., Ohshima, H., Aoki, S., Kawaguchi, S., Yamanouchi, T., Makino, Y., and Murayama, H., Variations of atmospheric carbon dioxide concentration at Syowa station, (69°00'S., 39°35'E.), Antarctica, *Tellus*, v. 39B, p. 72–79, 1987b.

Tanaka, M, Nakazawa, T., and Aoki, S., Time and space variations of tropospheric carbon dioxide over Japan, *Tellus*, v. 39B, p. 3–12, 1987c.

Tans, P., Conway, T. J., and Nakazawa, T., Latitudinal distribution of the sources and sinks of atmospheric carbon dioxide derived from surface observations and an atmospheric transport model, *Journal of Geophysical Research*, v. 94, p. 5151–5172, 1989.

Tucker, C. J., Townshend, J. R. G., and Goff, T. E., African land-cover classification using satellite data, *Science*, v. 227, p. 369–375, 1985.